SINTERING AND DENSIFICATION BEHAVIOR OF NANOPARTICLE-INFILTRATED ALUMINA SCAFFOLDS

A Thesis Submitted to
the Graduate School of Engineering and Sciences of
İzmir Institute of Technology
in Partial Fulfillment of the Requirements for the Degree of

MASTER OF SCIENCE

in Materials Science and Engineering

by
Metin ÖZBEKLER

July 2023
İZMİR

We approve the thesis of **Metin ÖZBEKLER**

Examining Committee Members:

Prof. Dr. Sedat AKKURT
Department of Materials Science and Engineering/ İzmir Institute of Technology

Assoc. Prof. Dr. Onur ERTUĞRUL
Department Of Metallurgy and Materials Engineering / İzmir Katip Çelebi University

Ass. Prof. Dr. Fatih TOKSOY
Department of Mechanical Engineering/ İzmir Institute of Technology

14/07/2023

Prof. Dr. Sedat AKKURT
Supervisor, Department of the Materials Science and Engineering, İzmir Institute of Technology

Prof. Dr. Sedat AKKURT
Head of the Department of Materials Science and Engineering

Prof. Dr. Mehtap EANES
Dean of the Graduate School of Engineering Sciences

ACKNOWLEDGEMENTS

I am deeply grateful and would like to express my sincere appreciation to all the individuals who have contributed to the success of my thesis study.

First and foremost, I would like to extend my heartfelt thanks to my advisor, Prof. Dr. Sedat Akkurt, for allowing me to work in his laboratory and for his invaluable guidance and support throughout my thesis study. His expertise and mentorship have been instrumental in shaping my research.

I would also like to thank Prof. Dr. Muhsin Çiftçioğlu and Dr. Özlem Çağlar Duvarcı for their support in conducting dilatometric measurements. Their expertise and assistance have contributed significantly to the accuracy and reliability of my experimental data.

Furthermore, I would like to thank Prof. Emre Yalamaç and Sinem Tekin for their previous studies related to my thesis. Their research has provided valuable insights and laid my work foundationI want to acknowledge the support and help of the Lab-146 members, particularly Emre Erğen and Tuğçe Özmen Egesoy. Their collaboration and assistance have been invaluable in various aspects of my research.

I am also indebted to my colleagues and friends who have supported me. Special thanks to Çetin Meriç Güvenç, Ezgi Oğur, Gizem Kurt, Levent Karacasulu, Dr. Merve Günnar Karakaya, Mustafa Neşet Çınar, Öykü İçin, Sümeyra Çiğdem Sözer, Şahismail Güzelgün, Tuğçe Aybüke Arıca Güvenç, Uğur Kartal, and Utku Hatipoğlu for their encouragement and assistance.

I want to acknowledge the contributions of Dr. Adem Yavuz and Burcu Akdağ Çağlar from Iztech MAM for their assistance with dilatometric measurements, Işın Özçelik for XRD measurements, and Burcu Oğuz Kılıç, Mutlu Devran Yaman, and Zehre Sinem Yılmaz for SEM analysis.

Lastly, I would like to express my deepest gratitude to my dear mother, Asiye Kara, my dear father, Muzaffer Özbekler, and my dear brother, Taha Özbekler, for their unconditional love, unwavering support, and constant motivation. Their belief in me has been my driving force. I would also like to thank my girlfriend, Betül Aydemir, for her unwavering support and understanding throughout this challenging journey. To all those mentioned and the countless others who have played a role in my academic and personal growth, I am genuinely grateful for your contributions and support.

ABSTRACT

SINTERING AND DENSIFICATION BEHAVIOR OF NANOPARTICLE-INFILTRATED ALUMINA SCAFFOLDS

This study explores high-purity Alumina's sintering and densification behavior, specifically the CT3000 SG variation, which traditionally requires high temperatures for full densification. The goal is to lower processing costs by achieving densification at lower temperatures through nanoparticle infiltration. The process involves a two-step heat treatment and infiltration technique. Alumina scaffolds are initially bisque-fired at 1100 °C and then infiltrated with a polymer precursor solution containing Al^{+3} ions, followed by decomposition at 400 °C to precipitate alumina nanoparticles in the scaffold pores. Multiple infiltration cycles are performed to enhance density. The relative density of furnace-sintered pellets increases with decreasing heating rate and increasing sintering temperature in reference samples. Infiltrated samples and "P" pellets (formed by washing CT3000 SG Alumina loose powder with the polymer precursor solution) follow a similar trend, with higher infiltration numbers leading to increased relative density. However, "P" samples have lower relative densities than reference samples. In-depth analysis using a horizontal dilatometer reveals that the 15 times infiltrated scaffolds exhibit better densification due to early activation of nanoparticles, leading to neck formation, reduced porosity, and altered particle shape. On the other hand, "P" pellets fail to achieve sufficient densification compared to reference samples. In summary, this study investigates lowering the sintering temperature of Alumina by nanoparticle infiltration. It involves bisque firing, multiple infiltration cycles, and a polymer precursor solution.

Results indicate that 15 times infiltrated scaffolds achieve better densification, while "P" pellets fall short of achieving adequate densification compared to reference samples.

ÖZET

NANOPARÇACIK SIZDIRILMIŞ ALÜMİNA İSKELELERİN SİNTERLENME VE YOĞUNLAŞMA DAVRANIŞLARI

Bu çalışma, yüksek saflıktaki Alumina tozlarının sinterleme ve yoğunlaşma davranışını incelemektedir; özellikle geleneksel olarak tam yoğunlaşma için yüksek sıcaklıklar gerektiren CT3000 SG varyasyonunu ele almaktadır. Çalışmanın amacı, nanoparçacık sızdırma yoluyla daha düşük sıcaklıklarda yoğunlaşma elde ederek fırın maliyetlerini düşürmektir. Çalışmada uygulanan işlem, iki aşamalı ısıl işlem ve sızdırma tekniği içermektedir. Alümina iskeleler başlangıçta 1100 °C'de bisküvi pişirilir ve ardından Al^{+3} iyonları içeren bir polimer öncü çözeltisi ile sızdırılır; ardından 400 °C'de çözeltinin ayrışmasıyla alümina nanoparçacıkların iskele gözeneklerinde çökelmesi sağlanır. Yoğunluğu artırmak için birden fazla sızdırma döngüsü gerçekleştirilir. Fırında sinterlenmiş pelletlerin bağıl yoğunluğu, referans örneklerde ısıtma hızının azalması ve sinterleme sıcaklığının artması ile artar. Sızdırılmış örnekler ve "P" pelletler (CT3000 SG Alümina gevşek tozunu polimer öncü çözeltisi ile yıkayarak oluşturulan pelletler) benzer bir eğilimi takip eder; daha yüksek sızdırma sayıları daha yüksek bağıl yoğunluk değerlerine yol açar. Bununla birlikte, "P" örneklerinin bağıl yoğunluğu referans örneklerden daha düşüktür. Yatay bir dilatometre kullanarak derinlemesine analiz yapıldığında, 15 kez sızdırılmış iskelelerin nanoparçacıkların erken aktivasyonuna, boyun oluşumuna, azaltılmış gözenekliliğe ve değiştirilmiş parçacık şekline sahip olmaları nedeniyle daha iyi yoğunlaşma elde ettiğini ortaya koymaktadır. Öte yandan, "P" pelletleri referans örneklerle karşılaştırıldığında yeterli yoğunlaşmayı elde edemez. Özetle, bu çalışma, Alümina'nın sinterleme sıcaklığını nanoparçacık sızdırma yoluyla düşürmeyi incelemektedir. Bu süreç , bisküvi pişirim, birden fazla sızdırma döngüsü ve bir polimer öncü çözeltisini içermektedir. Sonuçlar, 15 kez sızdırılmış iskeletlerin daha iyi yoğunlaşma elde ettiğini gösterirken, "P" pelletlerin referans örneklerle karşılaştırıldığında yeterli yoğunlaşmayı elde edemediğini ortaya koymaktadır.

TABLE OF CONTENTS

LIST OF FIGURES

Figure **Page**

Figure **Page**

Figure **Page**

LIST OF TABLES

Table **Page**

CHAPTER 1

INTRODUCTION

1.1. General Knowledge and Literature Review

Ceramics are non-organic materials produced by applying heat, sometimes in combination with pressure. They consist of at least two elements, one being a non-metal or a metalloid.[1] The additional element(s) in ceramics can indeed be metal(s) or another metalloid(s). In general, ceramics exhibit properties such as high thermal stability, hardness, chemical stability, corrosion resistance, electrical insulation, and resistance to high temperatures. However, they are inherently brittle. Indeed, in the literature, various studies focus on microstructural design and toughening mechanisms aimed at enhancing the fracture toughness of ceramics. These efforts seek to address the inherent brittleness of ceramics and make them more resistant to fracture and mechanical failure. Ceramics can be classified into two main groups: conventional and advanced. Conventional ceramics include structural clay products, pottery, clay-based refractories, cement, concrete, and glass. Advanced ceramics encompass ceramics used in various specialized applications such as electrical, magnetic, electronic, and optical fields (commonly known as functional ceramics). They are also utilized for structural purposes in both normal and high-temperature conditions (commonly known as structural ceramics).[2] Some examples of advanced ceramics are Zirconia (ZrO_2), Alumina (Al_2O_3), Titania (TiO_2), Silicon Nitride (Si_3N_4), Silicon Carbide (SiC), and Barium Titanate ($BaTiO_3$).

Ceramics have high melting points, primarily due to their structures' combination of ionic and covalent bonds. For instance, alumina (Al_2O_3) has a melting point of approximately 2072°C, and its sintering temperature is higher than 1500 °C. It takes a lot of energy to break most of the bonds to melt alumina partially. As a result, ceramics cannot be produced through conventional melting and casting techniques like metals. It is not practical and economical in terms of energy cost. Moreover, ceramics exhibit brittle behavior in terms of mechanical properties. This brittleness arises from insufficient active slip systems, the nature of the bond in their structure, and their sensitivity to defects in the microstructure. Due to these characteristics, ceramics cannot be produced using plastic-forming methods like metals. Powder processing methods are widely used in

ceramics manufacturing to address these obstacles. This process typically entails compacting ceramic powders into the desired form, subjected to high-temperature treatments like sintering or firing. Powder processing provides the ability to manipulate the microstructure of ceramics, offering control over their properties. Moreover, it enables the production of intricate and sophisticated shapes and structures in ceramics that would otherwise be challenging to achieve using alternative techniques. Since the starting material in powder processing is powder, the characteristics of powders are essential. The desired properties of the final component influence the selection of ceramic starting powders. The resulting properties of the ceramic material can be affected by parameters such as purity, particle size distribution (PSD), reactivity, and polymorphic form.[3] Therefore, careful consideration is given to these factors when choosing the appropriate ceramic starting powders. On the other hand, the most crucial step in powder processing is sintering. During sintering, powder particles undergo a heat treatment at high temperatures(below the melting temperature), resulting in their fusion and forming a solid material with a lower porosity.

In 2022, the global advanced ceramics market reached US$ 59.09 billion. It is projected to grow at a compound annual growth rate (CAGR) of 5% during the forecast period from 2023 to 2032, eventually reaching a market value of USD 95.79 billion by 2032.[4] In 2022, alumina emerged as the leading material in the global advanced ceramics market, representing a value share of 35% for that year. To ensure the dependable manufacturing of components in the advanced ceramics market, it is crucial to employ high-purity raw powders that exhibit reliable sintering and densification behavior.[5] To achieve cost-effectiveness in production, lower sintering temperatures are desired. This objective is accomplished by utilizing starting powders characterized by their high surface area and small particle size.[5] Consequently, there is an increasing requirement in the technical ceramics industry for fine-grained(1 μm>) high-purity powders.[5] In addition, alternative methods used for reducing the sintering temperature of alumina in the literature will be given in this section. The best example of sub-micron-grained, high-purity powder is CT3000 LS SG Alumina powder(Almatis). The utilization of Al_2O_3 powder extends to a broad range of product manufacturing. These applications encompass a wide range of products, such as alumina laboratory ware, porcelain crucibles, metal casting molds, high-temperature cement, wear-resistant components like tiles and sleeves, sandblast nozzles, seals, armor, medical parts, abrasives, refractories, and various other

ceramic pieces.[3] Al_2O_3 powder is highly regarded for its versatility and advantageous properties, making it a valuable material across multiple industries.

Two primary methods can be employed to improve the sintering kinetics or decrease the sintering temperature for Al_2O_3. The initial approach focuses on enhancing powder processing by utilizing fine-starting powders and eliminating agglomerates in their initial forms. This can be achieved through methods such as colloidal routes.[17,18,19,20,21] The second approach involves incorporating sintering aids or additives. When present in solid solutions, these additives can enhance diffusion and facilitate sintering by increasing the populations of defects within the material.[22,23] In contrast, additives that create a liquid phase can facilitate the rearrangement of particles and promote solution/reprecipitation processes.[24] As noted earlier, sub-micron grain-sized α-alumina powder has been widely adopted to prepare alumina ceramics.[6] This powder type can achieve densification at a relatively low temperature of approximately 1300 °C.[7] To achieve even lower sintering temperatures, sintering aids like silica, magnesia, titania, and yttria can be incorporated. These aids facilitate the transfer of matter between alumina particles, leading to accelerated densification of the alumina ceramic.[8,9,10,11,12,13] However, the incorporation of sintering aids may harm the mechanical properties of the ceramics by introducing new phases.[11,13] Therefore, the benefits and drawbacks of using sintering aids should be carefully considered.[13] Along with other techniques, the sol-gel process fabricates alumina ceramics due to its ability to achieve lower sintering temperatures.[13,14,15,16] However, the sol-gel process has its drawbacks, including a lengthy preparation cycle due to the low ceramic yield of the alumina sol and the propensity for shrinkage and cracking in the resulting ceramics.[13]

As an alternative to the previously mentioned approaches, Anderson [25] and his colleagues have proposed a two-step sintering and infiltration process to decrease the sintering temperature of ceramics utilized in solid oxide fuel cells. This method aims to enhance the performance and efficiency of fuel cell ceramics by reducing the required sintering temperature. The pellet used in this study is bisque fired at a temperature lower than the sintering temperature, leaving 50-60 % pores in the structure. Then, the polymeric precursor solution containing salts with the same composition as the host material infiltrates the porous pellet by infiltration technique. The pellet is subjected to heat treatment at 400 ^oC in the next step. The polymeric part is expected to move away from the structure and the nanoparticles to precipitate into the pores of the structure. Nanoparticles will be reactive at the sintering temperature due to their fine grain size and

high surface area, leading to premature densification. In this study, the sintering temperature of alumina was tried to be reduced by following a similar strategy. At the same time, the densification and sintering behaviors of the pellets were examined by constantly monitoring them with a dilatometer.

1.2. Motivations

The main motivations of this thesis are

- To reduce the sintering temperature of alumina.
- To investigate and characterize the densification and sintering attitude of non-infiltrated pellets and infiltrated alumina scaffolds.

1.3. Thesis Outline

The thesis investigates alumina powder's sintering, densification, and microstructural behavior in two forms: infiltrated scaffolds and non-infiltrated pellets. The specific alumina powder used in the study is the CT3000 LS SG, a commercially available product known for its relatively high purity. The study is categorized into a few chapters to facilitate understanding and presentation. The 2nd chapter is a preliminary section, providing relevant knowledge from existing literature. This literature review aims to help readers grasp the context and establish a foundation for comprehending the subsequent chapters. The third chapter details the experimental procedures employed in the study. This section outlines the specific methods and techniques for sintering, densifying, and characterizing the alumina powder, infiltrated alumina scaffolds, and non-infiltrated pellets. It provides a comprehensive account of the experimental setup and the steps to ensure accurate and reproducible results. The fourth chapter presents the findings related to the sintering and densification behavior of the alumina powder, infiltrated alumina scaffolds, and non-infiltrated pellets. This chapter encompasses the results obtained from powders, infiltrated scaffolds, and non-infiltrated pellets, allowing for a comprehensive comparison and analysis of their properties. Various factors influencing the sintering and densification processes are discussed in detail. Finally, the fifth chapter concludes the thesis by summarizing the essential findings and their implications. This section comprehensively explains the conclusions drawn from the

experimental results and provides insights into the overall behavior of the alumina powder, infiltrated, and non-infiltrated pellets. The findings are supported by the data presented in earlier chapters and aim to contribute to the existing knowledge in the field. Overall, the thesis delves into alumina powder's sintering, densification, and microstructural behavior, explicitly investigating the differences between infiltrated scaffolds and non-infiltrated pellets. The chapters are structured to provide a coherent and informative progression of the research, allowing the reader to follow the study with ease and understand the significance of the findings.

CHAPTER 2

BACKGROUND INFORMATION

This section will provide details on various topics, including ceramic materials, the properties of alumina, powder processing, properties of powders, sintering theory, the use of a dilatometer for monitoring the sintering of ceramics, and lastly, the infiltration process.

2.1. Ceramic Materials

Ceramics are materials created from inorganic, nonmetallic substances and are shaped first and then hardened through heat application.[26] The term "ceramics" originates from the Greek word "keramikos," which translates to "pottery" or "burned stuff." An older Sanskrit root also signifies "substance developed with the aid of fire." [26] This inclusive definition covers a broad spectrum of materials, including glass, refractories, porcelain, structural clay products, enamels, abrasives, cement, and pottery.[26] Furthermore, it encompasses ferroelectrics, non-metallic magnetic materials, glass ceramics, manufactured single crystals, and various other products within its scope. Ceramics possess several main characteristics, including brittleness, hardness, chemical stability, and thermal stability. [5]

Ceramics exhibit two primary types of bonds: ionic and covalent bonding. Ionic bonds occur between a metal and a nonmetal, where the electronegativity difference between the two elements is significant. In ceramic materials, mainly oxides, the ionic bond is predominant. [27] Covalent bonds, on the other hand, occur between two nonmetal atoms with similar electronegativity. Both ionic and covalent bonds in ceramics contribute to their unique properties. [27] These properties include high melting points, hardness, excellent chemical resistance, and low thermal expansion. Nevertheless, ceramics also possess specific undesirable characteristics, with brittleness. The inherent brittleness of ceramics makes them susceptible to fracture. Overall, the combination of ionic and covalent bonding in ceramics imparts specific qualities to these materials, enabling a wide range of applications while presenting challenges related to their structural integrity. Ceramics typically possess a crystalline structure, except for

amorphous glasses. [27] The crystal structure of ceramics and their properties can be influenced by the presence of electrically charged ions and the magnitude of the electrical charges on each ionic component. [27] Pauling's rules, as presented in Table 2.1, have been established to rationalize the crystal structures of ionic compounds in ceramics. These rules provide guidelines for understanding and predicting the arrangement of ions in the crystal lattice of ceramic materials.[27]

Table 2.1. Pauling's rules [28]

Cation-Anion Coordination	The cation-to-anion radius ratio should specify the coordination number of the cations.
Electrostatic Valency Principle	The sum of the electrostatic valencies of the cations and anions in a crystal structure should be equal.
Packing Principle	The packing of ions should maximize the strength of the ionic bonds and minimize repulsion between like-charged ions.
Electrostatic and Geometric Stability	The crystal structure should have a balance between electrostatic and geometric stability.
Coordination Polyhedra	The coordination polyhedra around each ion should be geometrically favorable and maximize ionic packing efficiency.

2.2. Classification of Ceramics

Ceramic products can be classified in various ways depending on different factors. Some classification schemes consider the coarseness or fineness of the ceramic product, while others focus on the specific functions expected from ceramics. A more general categorization separates ceramics into two main titles: "Classical" ceramics and "Engineering" ceramics.[26] Categorization of ceramics is given in Figure 2.1. Classical ceramics are primarily made from "triaxial" clay, quartz, and feldspar mixtures. These raw materials are sourced directly from nature. Quartz consists mainly of SiO_2, clay is an aluminosilicate mineral with the chemical formula $Al_2O_3.2SiO_2.nH_2O$, and feldspar is typically a potassium-based mineral with the chemical formula $K_2O.Al_2O_3.6SiO_2$.[26] For practical purposes, triaxial ceramics can be combinations of the oxides K_2O, Al_2O_3, and SiO_2. A grasp of the ternary phase diagrams in the K_2O-Al_2O_3-SiO_2 system is crucial for understanding the reactions during these ceramics' firing process. These diagrams provide valuable information about the phase compositions and transformations that occur due to changes in temperature and composition within the system. Examples of products in this

category include porcelain, china, tiles, earthenware, sanitary ware, and utilitarian ceramics.[26]

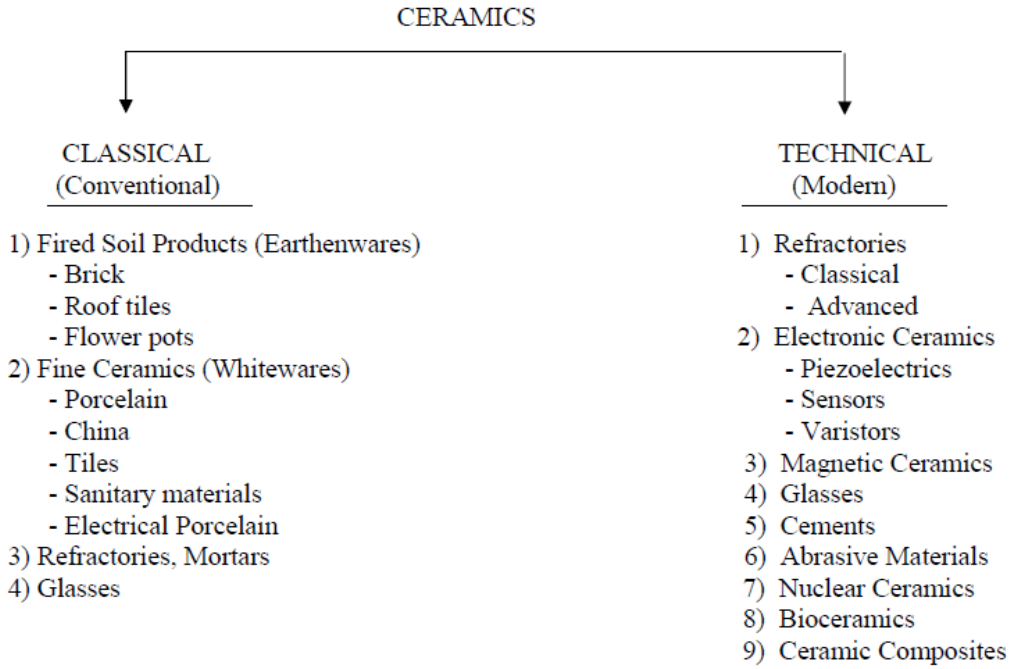

Figure 2.1. Classification of ceramic products in classical or technical base.[26]

On the other hand, technical ceramics are predominantly non-triaxial and are primarily manufactured using synthetic raw materials. These ceramics are designed for specific applications in electrical, electronic, magnetic, optical, mechanical, chemical, nuclear, thermal, biological, and structural fields. They can be formed from oxides such as TiO_2, ZrO_2, SiO_2, SnO_2, ZnO, PbO, NiO, CoO, Cr_2O_3, B_2O_3, Al_2O_3, MgO, CaO, and non-oxides. Non-oxide ceramics include carbides such as UC_2, SiC, B_4C, TiC, WC, UC nitrides like, and BN, Si_3N_4, and AlN borides such as TiB_2, ZrB_2, silicides like $MoSi_2$, and halides such as CaF_2, and SrF_2, NaCl, $MgCl_2$.

2.3. Alumina

Alumina(Al_2O_3) is a significant material in structural ceramics. The material has attracted considerable attention due to its exceptional properties, which include excellent abrasion resistance and a high melting point.,hardness, oxidation resistance, and corrosion resistance.[29] Some of the thermal and mechanical properties of α-Alumina are given in

Table 2.2. In the past, it found widespread use in various industrial applications such as aerospace, automotive, microelectronic, energy, and catalytic sectors.[28,29]

Table 2.2. Some of the thermal and mechanical properties of α-Alumina [42]

Property	**Value**	**Property**	**Value**
Tensile Strength(MPa)	117-173	Melting Point(^{o}C)	2051+/-9.7
Bending Strength(MPa)	307-413	CTE at 200-1000 ^{0}C(1/^{o}C)	$8.8*10^{-6}$
Compressive Strength(MPa)	1600-3733	Boiling Point (^{o}C)	3530+/-200
Modulus of Rigidity(G)$*10^{8}$ (MPa)	8.67-11.3	Hardness on the Mohs Scale	9
Modulus of Elasticity(E)$*10^{8}$ (Mpa)	21.7-26.8		

It remains applicable in optoelectronic, electronic, and fine metallurgical sectors.[30,31] Additionally, α-Al_2O_3 has extensive applications in traditional and advanced ceramic fields. It is a crucial substrate for developing semiconductors and superconductors using molecular beam techniques.[32]

Alumina exists in two forms: transition or metastable phases. The stable phase is α-Al_2O_3, while the metastable phases, including chi (χ), eta (η), kappa (κ), theta (θ), delta (δ), and gamma (γ), depending on the synthesis temperature.[33] Traditional methods to produce α-Al_2O_3 involve solid-state, thermally influenced transformations from aluminum oxide hydrates.[29] The extent and completeness of the transformation into the corundum structure depend on the duration and temperature of the thermal treatment.[33,35] Traditionally, using the Bayer process, bauxite has been the primary raw material for alumina production. The flowchart of the Bayer process is shown in Figure 2.2. However, non-bauxitic treatments, which are more common in many countries, have been developed as alternative methods for producing alumina. These treatments employ raw materials such as mica, alum, alunite, fly ash, and sillimanite to enhance the unconventional alumina production processes.[36,37] Overall, alumina ceramic, particularly in its α-Al_2O_3 form, possesses remarkable properties and finds diverse applications in various conventional and cutting-edge industries. The choice of production method and

raw materials can significantly impact the quality and characteristics of the alumina ceramic material.

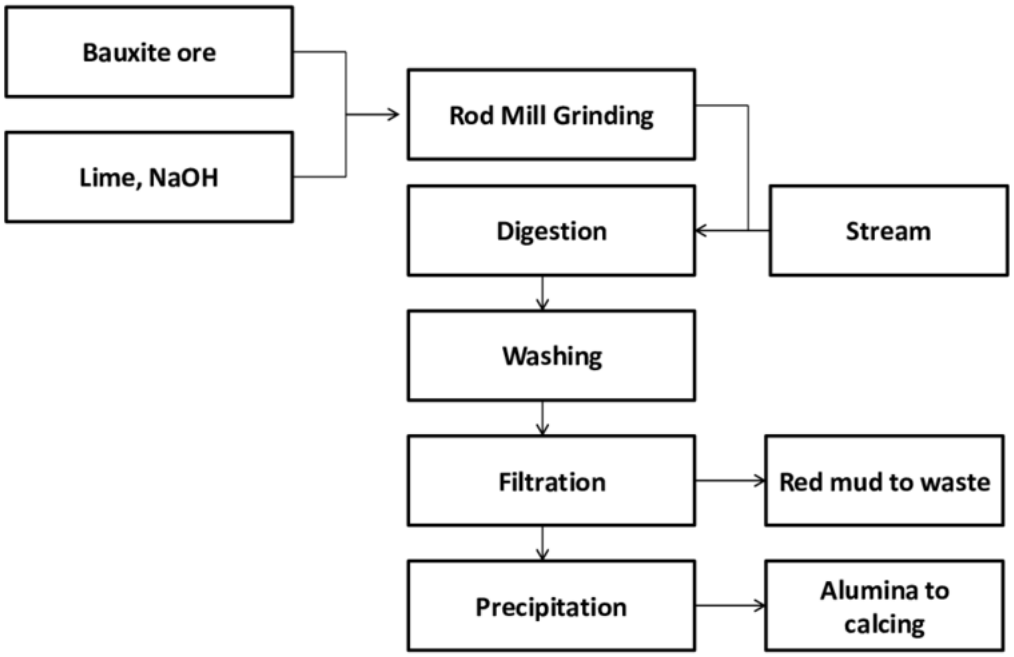

Figure 2.2. Flowchart of bayer process for alumina production [55]

The crystal structure of Al_2O_3 exhibits trigonal symmetry with the -3m crystal class.[39] Al_2O_3 possesses a pseudo-hexagonal oxygen sublattice, which accounts for the frequent use of a hexagonal cell and four-index Miller-Bravais notation. However, it is essential to note that the fundamental symmetry of the crystal structure is threefold, not sixfold.[39] In Al_2O_3, the oxygen ions are arranged like hexagonal close packing (hcp), while the Al^{3+} ions occupy two-thirds of the octahedral interstices to maintain charge balance. This arrangement results in a stable crystal structure with a specific ratio of aluminum to oxygen ions. [39] The crystal structure of α-Al_2O_3 is given in Figure 2.3.

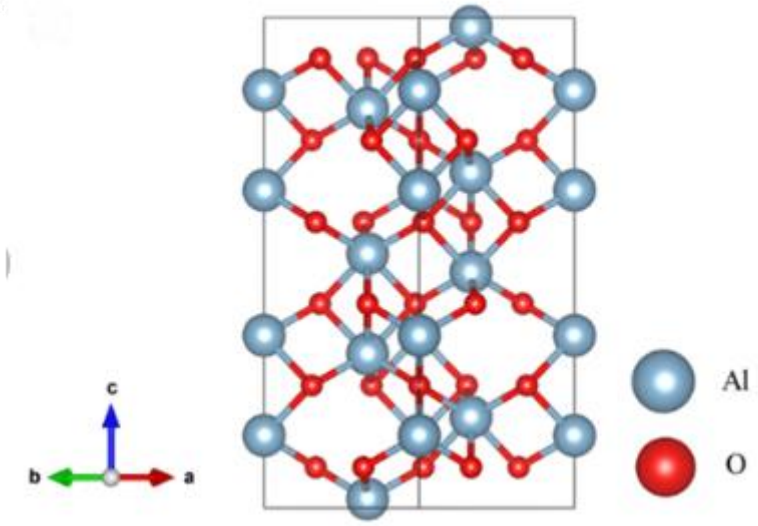

Figure 2.3. Hexagonal crystal structure of aluminum oxide (α-Al_2O_3) [40]

α-Alumina, or aluminum oxide (Al_2O_3), is the oxidized state of aluminum metal. Due to this oxidation, it is a stable phase, which limits the occurrence of further oxidation reactions. Strong ionic and covalent interactions characterize the bonding between Al^{+3} and O^{-2} ions in α-alumina. This unique bonding nature contributes to the material's hardness, high melting point, and resistance to corrosive acids. Some physical properties of α-alumina are shown in Table 2.3.

Table 2.3. Some physical properties of α-alumina.[41]

Property	**Value**
Crystallography	Hexagonal
Lattice Parameter, a	0.476 nm
Lattice Parameter,c	1.299 nm
Theoretical Density	3.986 g/cm^3
Thermal conductivity(298 K,99 %TD)	30 W m^{-1}K^{-1}
Specific Heat(298 K)	8-10*10^{-4} J Kg^{-1} K

2.4. Powder Processing

The powder processing route can involve several steps, the simplicity of which depends on the complexity of the process. In its basic form, this method consists of two main parts: the pre-sintering processes of the green article and the processes that take

place during sintering. The initial part involves the consolidation of fine particles (powder) to create a shaped and porous article, commonly known as a green body or powder compact. [2] Subsequently, the green body is subjected to the second phase of the process, wherein it is heated to a suitable high temperature (sintered) to promote densification and generate a final product with high density.[2] Recently, the primary emphasis and research endeavors have primarily focused on comprehending the processes that occur during sintering. These studies have provided valuable insights and knowledge, thereby contributing to the broader understanding of the powder processing route.[2]

2.4.1. Raw Material Selection Criteria

Indeed, the selection of ceramic starting powders plays a crucial role in determining the properties of the resulting ceramic component. Several criteria should be considered when choosing the starting powders, focusing on the desired properties of the finished part.[2] The critical criteria include:

Purity: The starting powders should have a high purity level to ensure the absence of impurities that may adversely affect the final ceramic's properties. Impurities can introduce defects, reduce mechanical strength, or alter the material's chemical and physical characteristics.

Particle Size Distribution (PSD): The particle size distribution of powders is vital for achieving desired microstructure and properties of the ceramic. A controlled and narrow PSD can lead to uniform densification during sintering, improving thermal and mechanical properties.

Reactivity: The reactivity of starting powders refers to their ability to react during processing and influence the final properties chemically. Some ceramic systems may require highly reactive powders to facilitate densification and enhance the desired phase formation.

Polymorphic Form: Certain ceramic materials exist in different polymorphic forms, where the crystal structure varies. The selection of the suitable polymorphic form of the starting powders is crucial as it can significantly impact the material's properties, including strength, electrical conductivity, and thermal stability.

By considering these selection criteria from the outset, it becomes possible to optimize the powder characteristics for the intended application and ensure that the final ceramic component exhibits the desired properties.

2.4.2. Powder Consolidation

The process of shaping ceramic powders to create a green article with the desired form is known as forming.[2] The primary techniques used for forming ceramics include:

Dry or Semidry Powder Pressing: This method involves compacting a dry or slightly moist ceramic powder into a desired shape using a die or mold.[2]

Colloidal-Based Methods: These methods utilize concentrated suspensions or slurries to consolidate the ceramic powders into the desired form. Examples of such techniques are slip casting and tape casting.

Plastic Forming Methods: In these methods, a paste-like mixture consisting of ceramic powder, water, and organic polymers is shaped through pressing or deformation**.** Extrusion is an example of a plastic forming method, where the ceramic paste is forced through a die to obtain a continuous profile.[2]

These forming methods offer different ways to shape ceramic powders, providing flexibility in achieving the desired geometry and structure for subsequent processing steps.

2.4.3. Sintering Process

After drying and potential debonding, the green article is exposed to a controlled heat treatment process. This process is carried out to transform the paste-like mixture into a solid material with the desired microstructure, making it suitable and functional for its intended purpose. The theory of sintering is explained in Section 2.5.

2.5. Theory of Sintering

The sintering process holds significant importance in the production of ceramics. Sintering is essential for achieving the desired microstructure and properties in almost all ceramic bodies. [5] The extensive use of the sintering process has resulted in the

development of various approaches and techniques within this field.[5] When a ceramist aims to create a material with specific properties, they first identify the desired microstructure that will enable those properties to manifest.[5] The primary goal of studying sintering is to comprehend the impact of processing variables on the evolution of microstructure during the sintering process.[5,43] By acquiring a more profound understanding of these relationships, valuable insights can be gained to aid in the practical task of designing optimal processing conditions that lead to the desired microstructure in ceramic materials.[5,43] This knowledge allows for more effective control and manipulation of the sintering process, producing the desired properties and performance of ceramics.[5,43]

2.5.1. Solid State Sintering

To convert the dried and debound green article into a solid material with the desired microstructure, it undergoes a controlled heat treatment known as sintering. In the case of a pure, single-phase material such as Al_2O_3, the sintering process consists of heating the green compact to a temperature range of approximately 0.5 T_m to 0.75 T_m.[2] For example, in the case of Al_2O_3 with a melting temperature of 2072 °C, the typical sintering temperature ranges from 1410 °C to 1660 °C. During sintering, the powder particles within the green article do not melt. Instead, the particles join together, and the porosity of the article reduces through mass transport in the solid state.[2] The process of sintering, in which densification and particle bonding occur without complete melting, is commonly known as solid-state sintering.

2.5.2. Liquid Phase Sintering

Liquid-phase sintering is a method where a viscous liquid is present during sintering, and it is the elementary mechanism for densification in most silicate systems, often in conjunction with viscous composite sintering.[3] Three parameters influence the rate of liquid-phase sintering:

1. Particle size
2. Viscosity
3. Surface tension

The composition and temperature of a liquid significantly affect its viscosity and surface tension. Optimal liquid-phase sintering occurs when the liquid phase thoroughly wets the solid particles during the sintering temperature. The fluid in the narrow channels between the particles creates considerable capillary pressure.[3] This capillary pressure facilitates densification through various mechanisms, including:

A-Particle rearrangement: The presence of liquid allows for the rearrangement of particles, facilitating better packing and closer contact between them. This leads to improved densification and reduced porosity.[3]

B-Increased contact pressure: The presence of the liquid phase enhances the contact pressure between particles, facilitating material transfer through various mechanisms. These mechanisms encompass solution and precipitation, creep and plastic deformation, vapor transport, and grain growth. These processes contribute to densification by facilitating atomic or molecular movement and grain boundary migration.[3]

The temperature plays a vital role in the rate of liquid-phase sintering. In general, even a slight increase in temperature results in a substantial increase in the quantity of the liquid phase present during the sintering process. [3] This temperature-dependent behavior has implications for the densification process. In some instances, the increased liquid phase at higher temperatures can be advantageous as it promotes faster densification. The higher mobility of the liquid phase facilitates enhanced mass transport and particle rearrangement, leading to improved densification and reduced porosity.[3] However, in other cases, the excessive presence of liquid phase due to higher temperatures can have adverse effects. It can lead to excessive grain growth, reducing final product strength. Additionally, at very high temperatures, the liquid phase can cause the part to slump and deform, compromising its dimensional stability.[3]

2.5.3. Reactive Liquid Sintering

Reactive liquid sintering is a process where a liquid is present, serving a similar role as in liquid-phase sintering. [3] It provides the necessary driving forces for densification. However, in reactive liquid sintering, the liquid changes composition or completely disappears as it progresses or after completion.[3] Reactive liquid sintering utilizes the presence of a liquid phase, enabling similar densification mechanisms as

observed in liquid-phase sintering.[3] It facilitates particle rearrangement, mass transport, and other processes that contribute to densification. In contrast to liquid-phase sintering, the liquid phase in reactive liquid sintering is consumed through reactions occurring during the sintering process. This consumption of the liquid phase leads to distinctive advantages. The resulting material can exhibit excellent high-temperature properties, surpassing conventional sintering methods. In certain instances, the material produced through reactive liquid sintering can demonstrate the capability to be utilized at temperatures even higher than the temperature at which the sintering process takes place.[3] Reactive liquid sintering offers the opportunity to create ceramic materials with exceptional properties by harnessing the benefits of a transient liquid phase that reacts and transforms during the sintering process.

2.5.4. Driving Forces for Sintering

During the sintering process, the consolidation of a green compact occurs with a decrease in the system's free energy, primarily achieved by eliminating internal surface area.[2,5] The energy reduction occurs as solid-vapor interfaces are substituted with more stable solid-solid or solid-liquid interfaces, decreasing energy. Three potential forcing power contribute to this energy reduction:

a) Surface Curvature: Surface curvature plays a significant role in driving the sintering process when no external stress or chemical reactions occur. Curved surfaces inherently create an energy imbalance, promoting particle rearrangement and densification during sintering. [2,5]

b) Applied Pressure: In cases where chemical reactions are absent, external pressure typically serves as the primary forcing power during sintering, particularly when the pressure is applied consistently during a specific portion of the heating process. Surface curvature also plays a role in driving the process, although its contribution is generally less significant compared to external pressure in practical scenarios.[2,5]

c) Chemical Reaction: Chemical reactions between the components can also be a sintering force. The energy reduction caused by a chemical reaction is generally much more substantial than the forces generated by applied stress or surface curvature. Chemical reactions can facilitate atomic rearrangement, phase transformations, and the formation of new bonds, leading to densification and structural changes in the material.[2,5]

In summary, the driving force behind the sintering process is minimizing the system's free energy. This reduction can be achieved through surface curvature, applied pressure, or chemical reactions. While each driving force contributes to the sintering process, their relative significance depends on the specific conditions and materials involved.

2.5.5. Mechanisms of Sintering

Polycrystalline materials undergo solid-state sintering by moving atoms (or ions) along specific pathways, determining the sintering mechanisms.[44] Certainly, in sintering, it is crucial to consider that matter is transferred from regions with higher chemical potential to areas with lower chemical potential. This movement of matter is driven by the desire to establish equilibrium and minimize the overall free energy of the system.[44] Figure 2.4. illustrates the schematic representation of six distinct sintering mechanisms in polycrystalline materials involving a system of three sintering particles.

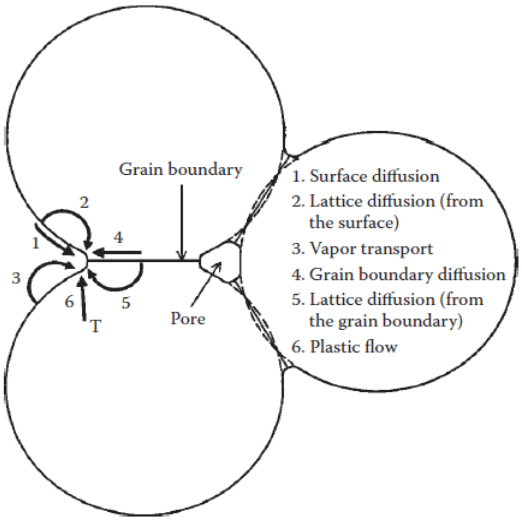

Figure 2.4. Six different mechanisms for sintering. [44]

Mechanisms 4-6 are the primary mechanisms responsible for densification during sintering. However, it is essential to note that all six mechanisms contribute to the growth of necks between particles. These necks play a crucial role in determining the rate of densification..[2,5,44] All of these mechanisms contribute to the formation of bonds and the growth of necks between particles, which ultimately increases the strength of the powder

compact during sintering. However, it is essential to note that only specific mechanisms are responsible for shrinkage or densification, while others do not directly contribute. As a result, a distinction is commonly made between densifying mechanisms, which promote shrinkage and densification, and nondensifying mechanisms, which primarily contribute to the bond formation and neck growth without significant densification.[44] Mechanisms 1, 2, and 3, namely surface diffusion, lattice diffusion from the particle surface to the neck, and vapor transport, contribute to the growth of necks between particles without causing significant densification. These mechanisms are referred to as non-densifying mechanisms. On the other hand, Mechanisms 4 and 5, which involve grain boundary diffusion and lattice diffusion from the grain boundary to the pore, are the primary mechanisms responsible for densification in polycrystalline ceramics. These mechanisms promote neck growth and facilitate densification by allowing material transfer from the grain boundary to the pore. Although Mechanism 6, plastic flow resulting from dislocation motion, also contribute to neck growth and densification, its importance in ceramic sintering is generally limited.[5,44]

2.5.6. Stages of Sintering

Coble suggested that solid-state sintering can be categorized into three stages, each representing a specific time interval or density range in which the material's microstructure is reasonably well defined. [5]

2.5.6.1. Initial Stage of Sintering

During the first sintering step, neck enlargement occurs between elementary particles through diffusion, vapor transport, and plastic flow. This leads to a rise in the surface area of interaction among the particles, beginning from an ideal point of contact and reaching a value of around 0.4-0.5 times the particle's radius.[43] In this stage, the significant differences in surface curvature are eliminated, and the material undergoes a linear shrinkage of around 3-5 %. Consequently, the material's density rises to approximately 0.65 times the theoretical density. It is important to note that during this initial stage, there is no significant grain growth, as observed by Coble.[43]

2.5.6.2. Intermediate Stage of Sintering

The intermediate stage of sintering begins when well-formed grain boundaries are present. Extensive grain boundary formation occurs in this stage while the pores remain interconnected, forming a continuous pore network.[43] At the same time, the grain boundaries remain isolated without forming a continuous network. Significant densification and microstructure changes characterize this stage. As the sintering process continues, the pores become sealed off. The grain boundaries establish an interconnected network. The intermediate sintering stage concludes when the material reaches approximately 0.9 of the theoretical density. Subsequently, the last step of sintering begins.[43,5]

2.5.6.3. Final Stage of Sintering

In the last step of sintering, closed pores are found at grain boundaries (interfaces) and triple junctions. Additionally, some pores may be entrapped within the grains themselves. Although the density increases slightly during this stage, the most significant development occurs in the microstructure, with rapid grain growth.[43,5]

2.6. Grain Growth Kinetics

Grain growth corresponds to the augmentation of average grain size in a multi-crystalline material. In ceramics, grain growth can be divided into two main types: normal and discontinuous. Normal grain growth occurs when the average grain size enhances with time while maintaining a self-similar grain size distribution, meaning that the distribution remains constant over time.[5] Discontinous grain growth includes the fast growth of a few large grains at the expense of smaller grains, resulting in a bimodal grain size distribution.[5] This process forms distinct groups of large and small grains within the material. The simulations conducted by Srolovitz [45] and Anderson [46] utilized a Monte Carlo method to simulate grain growth that incorporates topological constraints, resulting in realistic representations of the process. These grain growth models provide predictions based on a kinetic equation that follows a specific form:

$$(d)^m-(d_o)^m=Kt \quad (2.1)$$

d_o: Initial grain size (Primary crystallite size)

t: Soak time at specified sintering temperature

K: Constant,

m: Grain growth exponent ranging from 2 to 4.

is 2 for the normal grain growth, 3 for grain boundary segregation and

4 for grain boundary precipitation.

2.7. Continuous Monitoring of Sintering with a Dilatometer

A Thermal dilatometer is a highly accurate tool designed to track changes in the dimensions of materials concerning temperature.[48] It finds applications in testing diverse materials, including traditional and advanced ceramics, glasses, metals, and polymers.[48] Dilatometry provides a comprehensive range of measurements, including linear thermal expansion, coefficient of thermal expansion, sintering temperature, shrinkage steps, phase transitions, density change, softening point and decomposition temperature, anisotropic behavior, and glass transition temperature.[48] The horizontal dilatometer is shown in Figure 2.5.

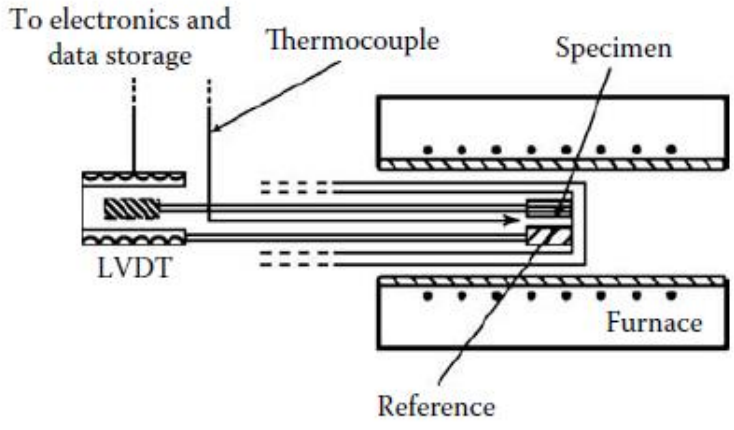

Figure 2.5. Schematic representation of horizontal dilatometer [44]

The pellet is placed in a dilatometer in a holder heated with a furnace. Using a push rod perpendicular to a pellet in conjunction with a Linear Variable Displacement

Transducer (LVDT) allows for the measurement of linear length changes.[5] As the temperature increases, the pellet undergoes length changes, which are saved as an output signal proportional to the displacement in the LVDT.[5] The temperature program is regulated by employing a thermocouple positioned either close to the heating element of the furnace or in the vicinity of the sample. In the dilatometer, the pellet and push rod undergo thermal expansion simultaneously. The dilatometer signal obtained is a sum of the length changes in the sample, sample holder, and push rod. To determine the change in length individually in the pellet, the lengthwise expansion information at the temperature at which the dilatometer operates without a pellet is subtracted from the overall length expansion. [5,50]

Lengthwise expansion:

$$\Delta L_{corrected} = \Delta L_{sample} - \Delta L_{blank} \quad (2.2)$$

The $\Delta L_{corrected}$ pellet undergoes lengthwise expansion, while the ΔL_{sample} pellet experiences the total lengthwise increase. It represents the change in length that occurs when the ΔL_{blank} dilatometer is operated at the desired test temperature.[5]

Thermal expansion coefficient:

$$\frac{\Delta L}{\Delta L_0} = \alpha \Delta T \quad (2.3)$$

In the equation, ΔL represents the length variation of the specimen, L_o denotes the original length of the sample, and ΔT corresponds to the change in temperature.

To comprehend the processes occurring during sintering, it is crucial to measure the sizes of grains and pores and the overall shrinkage of a powder compact, concerning sintering variables such as time, temperature, and initial particle size.[39] When a powder compact undergoes shrinkage, its density increases over time. Therefore, the most effective way to track densification is by measuring the density of the green compact as a function of sintering time, usually expressed as a percentage of the theoretical density.[39] This is commonly achieved through dilatometric measurements, where the length of a powder compact is monitored as a function of time at a specific temperature. Figure 2.6. illustrates typical shrinkage curves for two temperatures where T_2 is greater than T_1.

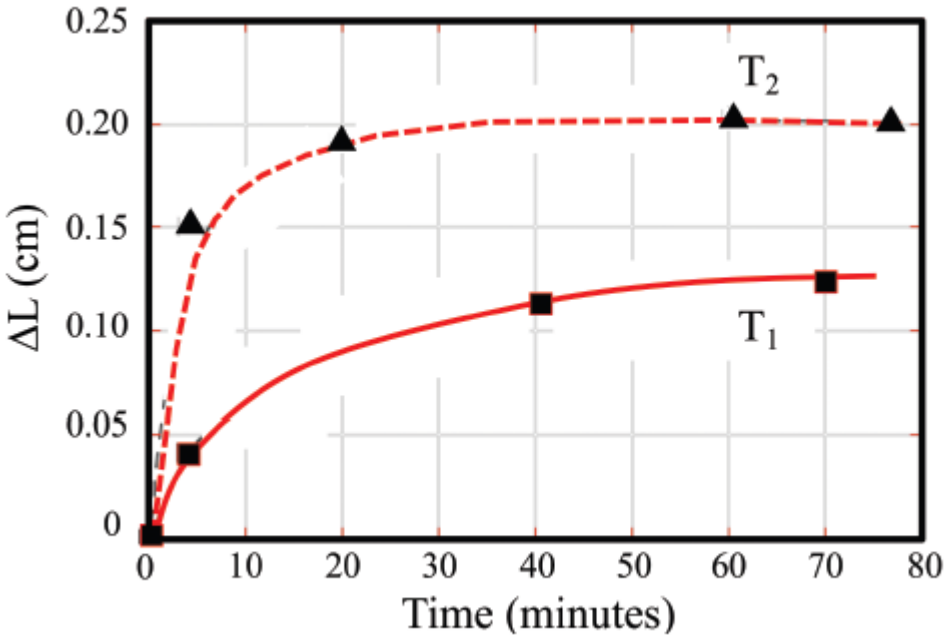

Figure 2.6. Typical shrinkage curves during sintering as a function of temperature where $T_2 > T_1$.[39]

2.7.1. Densification Rate Curves from Dilatometry

The kinetic information related to the densification process of a powder compact during sintering holds significant practical and theoretical importance. [2] These data can be obtained in two ways:

Intermittently: In this process, the density of the green compact is measured after being subjected to firing at defined temperatures for a specific period. The densification kinetics can be determined by analyzing density measurements at different intervals.[2,5]

Continuously**:** The technique of dilatometry is used in this method. The shrinkage ($\Delta L/L_o$), which is the change in length of the sample relative to its initial compact size, is measured using a dilatometer.[2,5] The instrument continuously collects data on shrinkage and temperature during the heating process. Shrinkage is a sign of the densification mechanisms, such as grain boundary diffusion.[51] However, it should be noted that coarsening processes coinciding can affect the driving force for densification .[51]

Densities, $p(T)$, and densification rate curves calculated from the shrinkage information and final density o_f measurements using the following equation:[5]

$$\rho(T) = \rho_f \left(\frac{1 + \frac{\Delta L_f}{L_o}}{1 + \frac{\Delta L_{(T)}}{L_o}} \right)^3 \tag{2.4}$$

In the equation, L_o represents the initial sample length, L_f represents the final sample length, and L(T) represents the sample length at temperature T.[52] After the samples were cooled, the final densities were measured using the traditional Archimedes' method. To calculate the rate of densification, the temperature derivative of the relative density (ρ) is taken. [5] This derivative provides information about how the density changes with respect to temperature, indicating the rate at which densification occurs.

$$\frac{d\rho_{(T)}}{dT} = -3 * \frac{d\left(\Delta L_{(T)} / L_0\right)}{dT} * \frac{\left(1 + \frac{\Delta L_{(f)}}{L_0}\right)^3}{\left(1 + \frac{\Delta L_{(T)}}{L_0}\right)^4} * \rho_f \tag{2.5}$$

2.8. Infiltration Process

In the sintering process of ceramics, the densification rate is directly linked to the surface area and fineness of the powder particles. Typically, the densification rate exhibits an upward trend when temperatures surpass half of the melting point of the ceramic material. [2] This suggests that higher temperatures contribute to more rapid densification, possibly due to enhanced diffusion and rearrangement of atoms or ions within the material. Achieving higher densities at lower temperatures in ceramic sintering offers several advantages, such as energy savings in kiln operations. Various studies have been conducted to enhance the sintering rate at lower temperatures, including using excellent starting powders and a two-step approach.[25,44,47]

The two-step method entails first sintering the initial powder compact to an intermediate temperature, typically achieving approximately 50-60 % of the theoretical density. This intermediate stage produces a porous scaffold, a semi-fired pellet. Nano-sized particles are then loaded (or infiltrated) into these porous ceramics to enhance the densification rate further.[25] Anderson and his colleagues initially introduced the concept of lowering the densification temperature of ceramics used in fuel cells. They created a porous scaffold filled with a polymeric infiltration solution and subjected it to a heat treatment at approximately 400°C. This heat treatment served the purpose of eliminating volatile components and causing salts to precipitate within the pores.[25]

In this approach, the porous ceramics act as a template for the infiltration solution, precipitating nano-sized powders within the pores, improving the densification rates. A polymeric solution is selected based on its superior wetting properties, enabling it to penetrate the pores.[25,47]. As the temperature increases, the salts precipitate as nano-sized particles within the pores. In the second heating stage, these nano-sized particles can quickly dissociate and transform into nano-sized oxide particles. Therefore, the two-step sintering process involves two steps: (1) Loading of the pores with nano-sized particles and (2) Second-stage heating to continue sintering of the porous scaffold. Indeed, nano-sized ceramics within the pores accelerates their activation during the sintering process compared to the main ceramic compact. This early activation contributes to enhanced densification and desirable material characteristics. Due to this early activation, the density of the material can increase even before reaching the final sintering temperature. In essence, the two-step sintering process divides the sintering into two stages, leveraging the presence of nano-sized ceramics to enhance densification at lower temperatures.

2.9. Capillary Action

Capillary action occurs due to the attractive forces between molecules in a liquid and a solid. The adhesive forces between the liquid and solid, along with the surface tension of the liquid (a consequence of cohesive forces within the liquid), can cause the fluid to move upwards in narrow spaces, such as capillary tubes.[56] The height to which the liquid rises, known as capillary rise, depends on factors such as the surface tension of the liquid, the contact angle between the liquid and solid, the perimeter available for the liquid to wet, the density of the liquid, and the force of gravity.[57] Porous ceramics

naturally draw in and hold fluids within their pores through capillary action. This characteristic renders them hydrophilic or water-attracting materials.[58] The charged surface of the ceramic's pores and channels facilitates the bonding and attraction of polar molecules, such as water and other fluids. [58] As a result, these ceramics exhibit the phenomenon of "wicking," wherein fluids are drawn into the material and transported through capillary forces.[58] The size of its pores directly influences the ceramic's air entry or bubbling pressure and hydraulic conductivity. [58] The tiniest opening within a channel or pore determines the adequate pore size, commonly known as the minimum orifice.[58] Therefore, polar polymer precursor solution with high surface tension and superior wetting properties will infiltrate the alumina scaffolds by capillary effect, depending on the pore size of the prepared alumina scaffolds.

CHAPTER 3

EXPERIMENTAL PROCEDURE

This section will introduce the experimental stages followed during the thesis and the materials and equipment used. Firstly, the physical and chemical characteristics of the CT3000 LS SG Alumina powder are introduced, and it was explained how the alumina pellets and porous scaffolds were prepared. In the next step, the infiltration experiments were clarified in detail. Then, the experiments performed in the box kiln and dilatometer were mentioned. Finally, weight and density measurements and characterization techniques were given, respectively. The steps followed while performing the experiments can be seen in Figure 3.1.

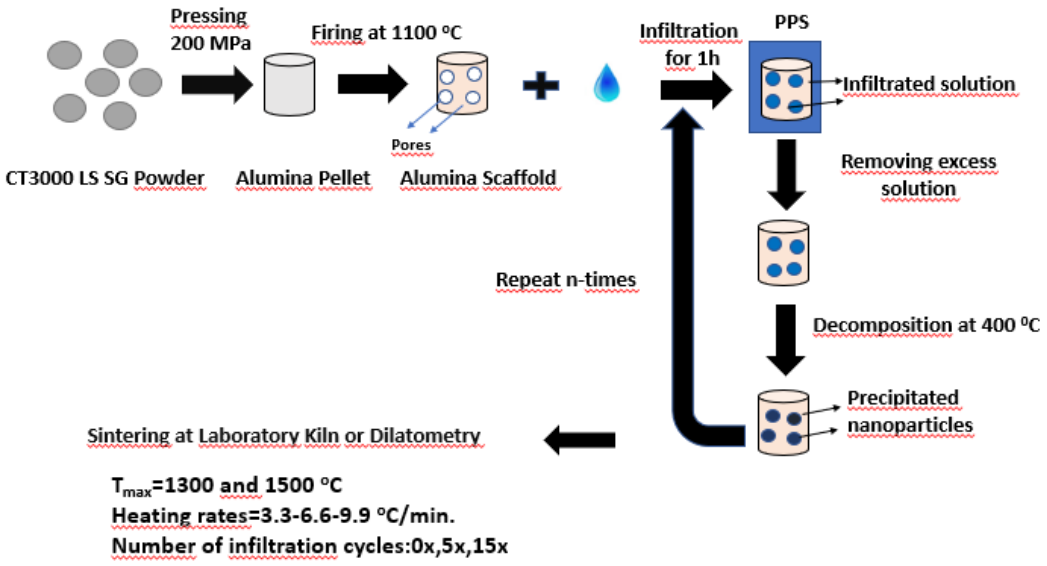

Figure 3.1. Schematic representation of the experimental steps followed in the thesis.

3.1. CT3000 LS SG Alumina Powder

Almatis Alumina CT3000 LS SG was used as starting material throughout this thesis. It is a low-soda-content advanced ceramic powder with high reactivity.[1] It has high purity of >99.9 % and high sintered density.[1]

Table 3.1. Chemical Properties of Almatis Alumina CT3000 LS SG[1]

Chemical Analysis	**[%] Typical**
Al_2O_3	99.8
Na_2O	0.03
Fe_2O_3	0.015
SiO_2	0.015
MgO	0.04
CaO	0.015

Table 3.2. Physical Properties of Almatis Alumina CT3000 LS SG[1]

Properties	**Typical**
Specific Surface area / BET	7.80 m^2/g
Particle Size / D50 Cilas	0.5 µm
Particle Size / D90 Cilas	2.0 µm
Green density (90 MPa)	2.24 g/cm^3
Fired density (1540 °C / 1600 °C)	3.91 g/cm^3 / 3.95 g/cm^3
Shrinkage (1540 °C / 1600 °C)	16.8 / 17.3

This powder is commonly used in high-end ceramic parts requiring high sintered density and high purity.[1] The theoretical density, surface area, and primary particle size of powder, as reported by the supplier, was 3.93 g/cm^3, 7,8 m^2/g, and 500 nm, respectively. The powder's other significant physical and chemical properties are shown in Table 3.1. and Table 3.2.

To better analyze the polymeric precursor solution infiltrated the scaffolds, the polymeric precursor was dried in an oven for 3 hours, and powder was obtained. The properties of this powder were subjected to the same characterization processes as the CT3000 LS SG Alumina powder.

3.2. Preparation of Alumina Pellets and Scaffolds

Samples prepared for dilatometer experiments should be in pellet form. For dilatometer experiments, how much powder we put into the mold is essential, as dimensional constraints exist on the pellet. If the dimensional restriction is not considered, incorrect measurements may be taken due to the contact of the pellet with the thermocouple. A study was conducted to determine how much powder we put in and what size was obtained by trial and error. As a result, when approximately 0.73 g of CT3000 LS SG powder is placed in the mold, a cylindrical pellet with a diameter of 8 mm and a height of 6 mm is obtained. This is the ideal pellet size for the dilatometric analysis.

Before pressing, a two-wt % Polyvinyl alcohol(PVA) solution is prepared. Polyvinyl alcohol (PVA) is an organic binder that provides some lubrication during pressing and gives the pressed part adequate strength for handling, inspection, and green machining.[2] Then, the CT3000 LS SG green powder is weighed on a precision scale and put into an agath mortar. As mentioned above, the CT3000 LS SG powder required for a pellet is approximately 0.73 g. two drops of the prepared PVA solution are taken with a pipette and dripped onto the powder, and the mixture of green powder and PVA solution is grounded.

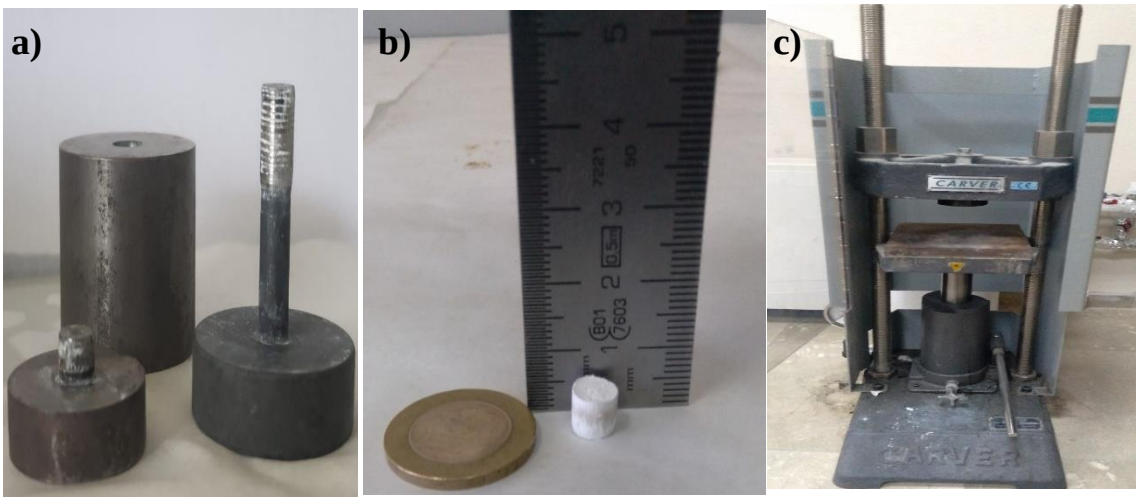

Figure 3.2. a) 1.2379 cold work steel die b) Alumina pellet c) Uniaxial Press(Carver)

A cylindrical die made of 1.2379 cold work tool steel with a diameter of 8 mm and a height of about 30 mm was used to pelletize the green powder. All pellets were

formed with a uniaxial hydraulic(Carver Hydraulic Press, Wabash Inc, USA) press at 200 MPa pressure. The die, pellet, and hydraulic press are shown in Figure 3.2.

After the pellets are prepared, they are bisque fired at a temperature lower than the actual sintering temperature, intentionally allowing the formation of pores in their structures. The pellet has approximately 50-60 % theoretical density in bisque firing. In other words, it contains 40-50 % porosity. The porous structure formed is called a "scaffold." Bisque firing will provide an advantage by handling the pellets and creating a porous structure for infiltration. To find the ideal bisque firing temperature, the pellets were subjected to heat treatment in the laboratory kiln at 900^0C, 1000^0C, and 1100 ^{0}C, and their strength was checked. As a result of these observations, it was seen that 1100 ^{0}C gave the best strength. Then, after the experiment on the soaking time, it was seen that soaking for 1 hour was ideal. For bisque firing of the pellets laboratory kiln(Nabertherm LHT02/17, Germany) is used.

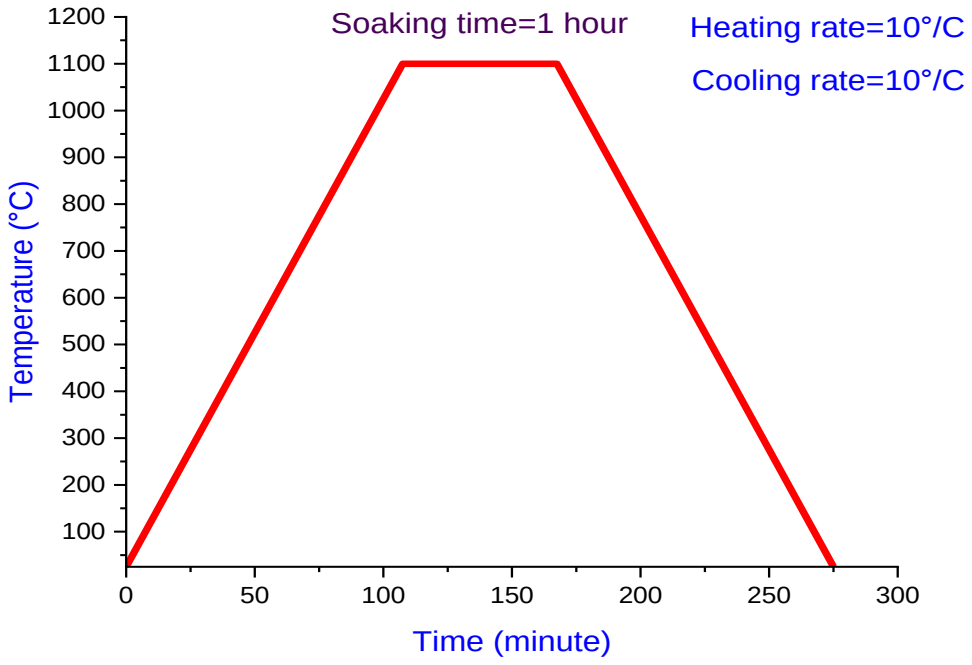

Figure 3.3. Sintering profile of the bisque-fired alumina pellets

The heating/cooling schedule to which the pellets are exposed during bisque firing is given in Figure 3.3.

3.3. Preparation of Polymeric Precursor Solution

The precursor solution was prepared by dissolving 15.56 g (Carlo Erba >99%) aluminum chloride hexahydrate salt with 200 g deionized water. Then, the solution formed is mixed with 200 g of ethylene glycol and combined in a magnetic stirrer so that the mole ratio of ethylene glycol and aluminum salt is 0.02.[53.] In the next step, the solution is stirred at 80 ^{0}C and 200 rpm, and the water is expected to evaporate. During this period, weight reduction is constantly checked. [54] Another thing to note is that the metal salt is a hydrated compound, so the water in the salt's structure must also be removed. After all the water evaporates, a non-aqueous and more viscous solution is obtained. To improve the wetting properties of this solution and decrease the surface tension of the solution, the solution is diluted by adding 2-butoxyethanol solution in a 1:1 weight ratio.[15] Procedure is summarized in Figure 3.4.

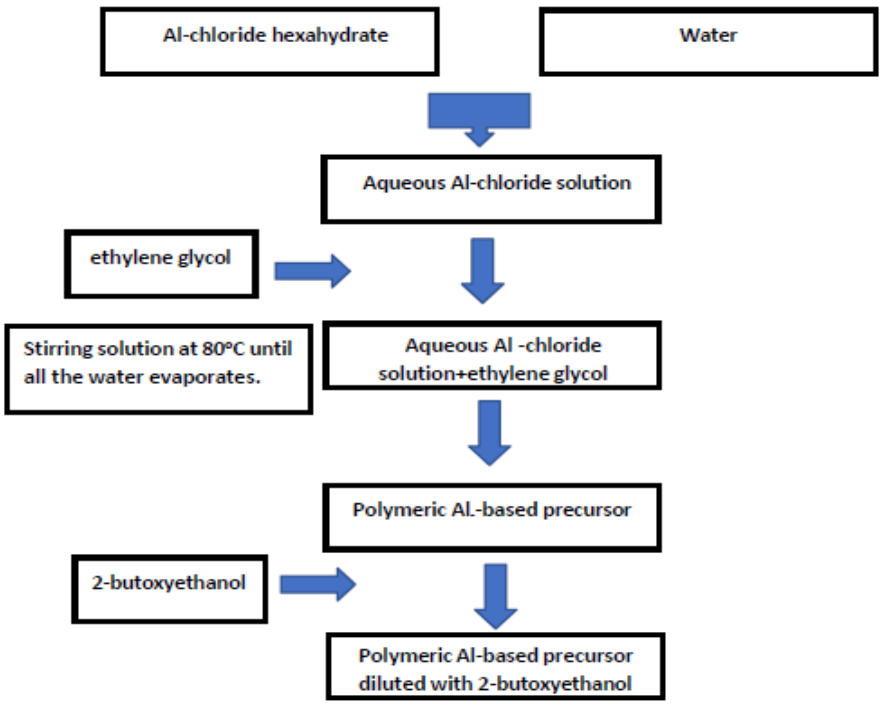

Figure 3.4. Preparation of polymeric precursor solution

3.4. Infiltration Experiments

To summarize the preparation of infiltrated samples, CT 3000 LS SG alumina powder is ground in agath mortar by dropping two drops of 2 % by weight PVA solution, which acts as a binder, as stated before. Then, after the powder and PVA mixture dry, the mixture is poured into a mold made of 1.2379 cold-worked tool steel, and pellets are formed with a uniaxial hydraulic press at 200 MPa pressure. The pellets formed are approximately 6 mm long and 8 mm in diameter. In this case, they are suitable for dilatometric measurement. Next, In this step, the pellets are sintered in the laboratory kiln at 1100 ^{0}C and 40-50 % porosity is formed in their structure. The pores formed in bisque-fired pellets host the Al-based polymer precursor solution to be infiltrated.

Regarding the infiltration stage, the bisque-fired pellet or alumina scaffold is placed in the Al-based polymer precursor solution in the double-necked flask. One end of the double-necked flask is connected to the vacuum pump(Lanphan 2XZ-2, Zhengzhou, Henan, China), and one is closed. The infiltration setup is shown in Figure 3.5. Then, the solution is ensured to infiltrate into the pellet within 1 hour. Each infiltration cycle in the experiments takes 1 hour.

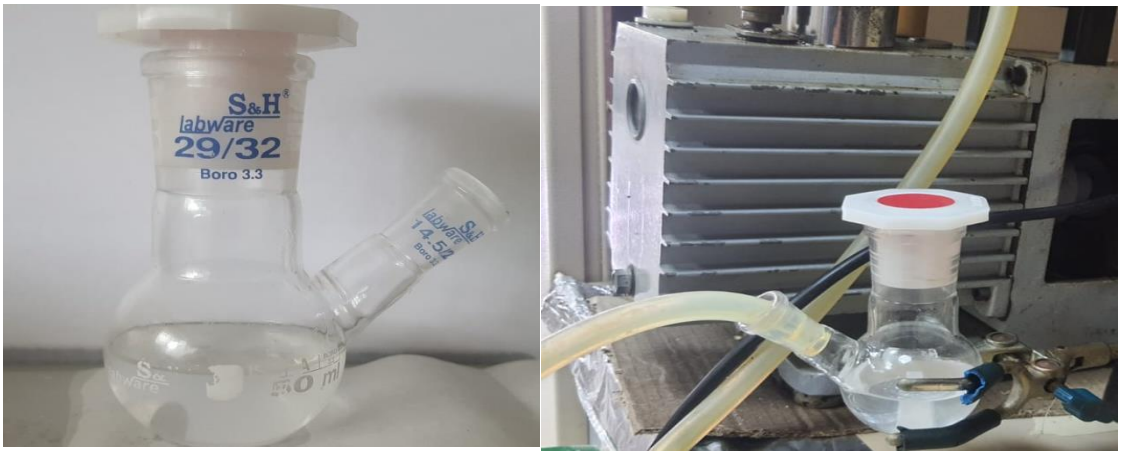

Figure 3.5. a) Immersed Alumina scaffold in the polymer precursor solution. b)Vacuum pump and infiltration setup

After the infiltration cycle is completed, since there is an excess solution on the pellet surface, the pellet is wiped with a damp cloth so that this solution does not dry out and forms a crust with an increasing infiltration cycle. The critical point here is that the

moisture rate of the cloth is well-adjusted. If a dry cloth is used, the cloth can altogether remove the solution in the alumina scaffold. After this stage, the polymeric part is removed by decomposition at 400 ^{o}C in the muffle furnace, and the nano-sized aluminium oxide particles precipitate into the pores of the alumina scaffold. After the deterioration of the polymeric part, an infiltration cycle is completed. If the number of infiltration cycles for that pellet is n, infiltration is repeated n times. Finally, infiltrated alumina scaffolds are sintered in a laboratory kiln or dilatometer. For sintering, two different temperatures, 1300 and 1500 ^{0}C, as well as three different heating rates, 3.3,6.6, and 9.9 ^{0}/min. used. There are three other sample groups. The first group is infiltrated samples. Infiltrated samples are named “AK” if they are sintered in a laboratory kiln and “AD” if they are sintered in a dilatometer. The preparation of infiltrated scaffolds is given in Figure 3.6.

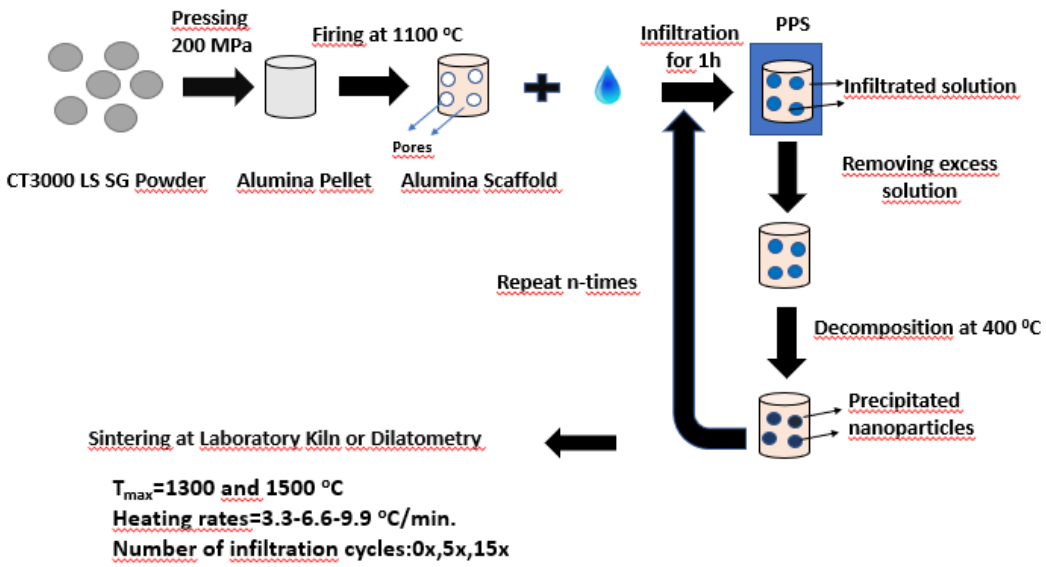

Figure 3.6. Schematic representation of the preparation of infiltrated scaffolds.

In infiltration, a vacuum pump removes the air trapped in the alumina scaffold's pores and replaces it with an Al-based polymeric precursor solution. Then, as mentioned above, the polymeric part and the solvent are decomposed at 400 ^{0}C, and the precipitation of alumina nanoparticles is aimed. The precipitation of nanoparticles is shown in Figure-3.7.

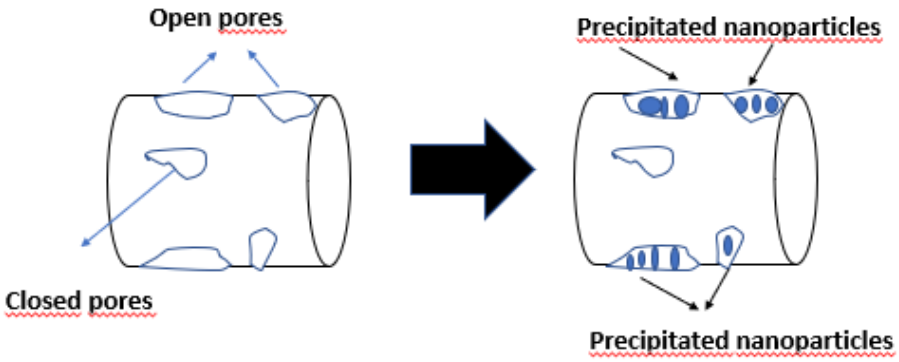

Figure 3.7. Demonstration of the porous alumina scaffold, evacuation of air pockets by a vacuum pump and infiltration of the polymeric precursor, then precipitation of nanoparticles after decomposition at 400 °C.

The second group is the pellet formed by polymer precursor solution coated loose powder. These samples are coded with the letter "P." CT 3000 LS SG alumina loose powder and Al-based polymer precursor solution are mixed in a beaker and left to dry in an oven at 250 ^{0}C for 3 hours.

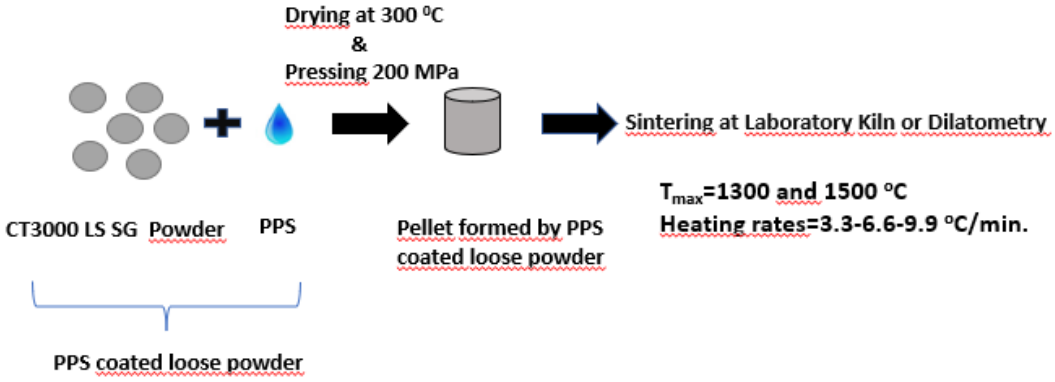

Figure 3.8. Creation of the pellets that are formed by polymeric precursor-coated loose powder

Then, loose powder coated with Al-based polymeric precursor solution is ground, and this powder is pressed with 200 MPa pressure to obtain pellets of the same size as the

other samples. For sintering, there are two different temperatures, 1300 and 1500 ^{0}C, and three different heating rates, 3.3,6.6, and 9.9 ^{0}/min. used. Creation of the pellets that are formed by polymeric precursor-coated loose powder is shown in Figure 3.8.

The third group samples are non-infiltrated reference pellets. These samples are coded with the letter "R." CT3000 LS SG powder is pressed with a pressure of 200 MPa in a hydraulic press. For sintering, two different temperatures, 1300 and 1500 ^{0}C, as well as three different heating rates, 3.3,6.6 and 9.9 ^{0}/min. used. Again, the pellets formed are approximately 6 mm long and 8 mm in diameter.

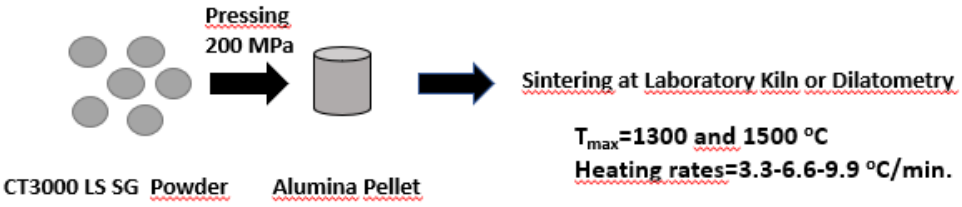

Figure 3.9. Schematic representation of the preparation of reference samples.

It is essential to characterize E-powder to investigate the presence of oxide nanoparticles at sintering temperatures. E-powder is the powder obtained by heat treatment of the prepared polymeric solution in an oven at 250 ^{0}C for 3 hours. E-powder is heat treated with a heating rate of 10 ^{0}/min. at 300, 500, 700,900,1100 and 1300 ^{0}C for a soaking time of 1 hour.

3.5. Heat Treatment Experiments

A laboratory kiln(Nabertherm LHT02/17, Germany) was used in sintering and bisque firing experiments. The samples were placed in an alumina crucible. Tabular alumina was sprinkled on the alumina crucible so there would be no friction between the pellets and the alumina crucible, and the pellet would not be damaged.

Figure-3.10. Laboratory kiln for sintering and bisque firing pellets

In the sintering experiments, the maximum temperatures are 1300 ^{o}C and 1500 ^{o}C, while the heating rates are 3.3, 6.6, and 9.9 ^{0}/min. The sintering profiles of the pellets are shown in Figures 3.11 and 3.12.

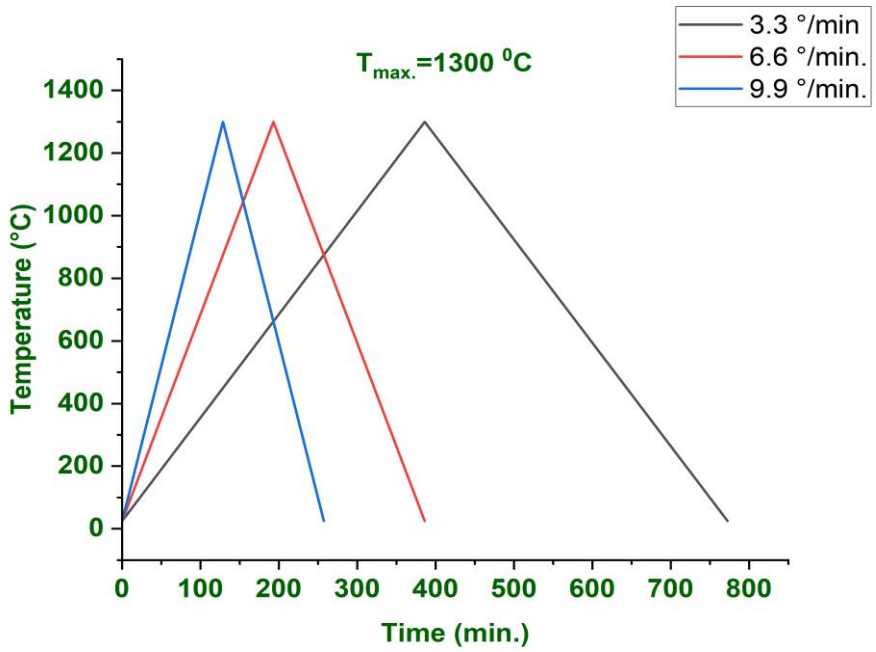

Figure 3.11. Sintering profiles of the pellets that are formed during the experiments ($T_{max.}$=1300 ^{0}C)

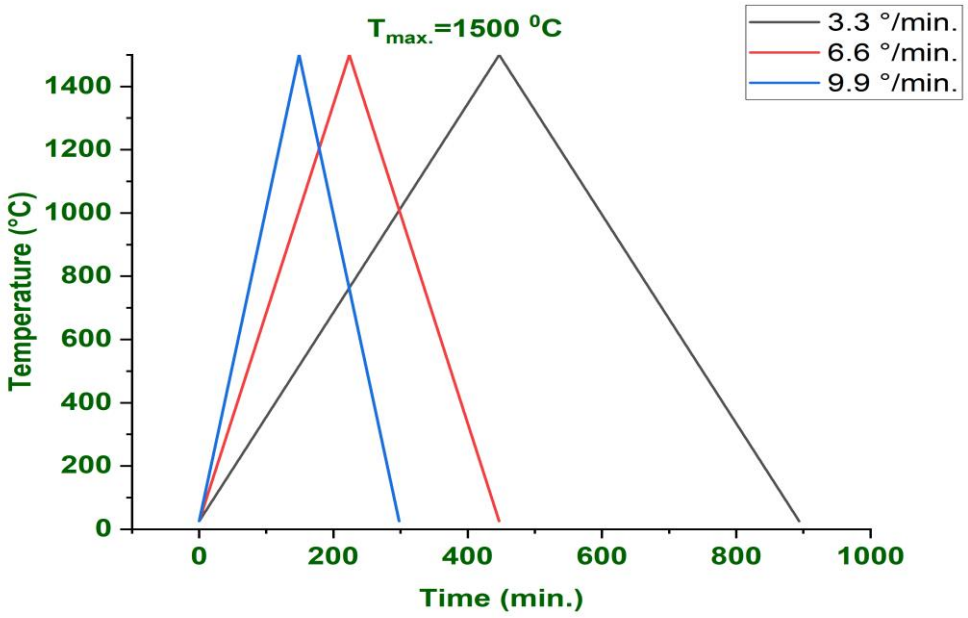

Figure 3.12. Sintering profiles of the pellets that are formed during the experiments ($T_{max.}$=1500 ^{0}C)

In the sintering experiments, soaking time is zero. Heating and cooling rates are constant. Therefore these types of profiles are called constant heating rate experiments.

A muffle furnace (Protherm1600) was used to apply the 400 ^{o}C heat treatment while preparing the infiltrated pellets. The main aim is to decompose the samples' polymeric part and evaporate the solvent. To carry out this process, the furnace is kept at 400 ^{o}C continuously. After the pellet is infiltrated for 1 hour in a vacuum environment, it is held at 400 ^{0}C in the muffle furnace for 1 hour. Thus, an infiltration cycle is completed. This process is repeated n times depending on the number of the infiltration cycle aimed. The Muffle furnace is shown in Figure 3.12.

Figure 3.13. Demonstration of the muffle furnace used for decomposing the polymeric part of the solution.

In this study, a dilatometer was used to monitor the sintering process of the pellets formed. This is a horizontal dilatometer(Linseis L76150B-1600), which can heat up to 1600 ^{0}C. The samples are sintered in air at constant heating rates from 1 to 10 ^{o}/min. up to 1500 ^{0}C without soaking time. This dilatometer applies a constant load of 0.1 N to the sample. Pellet dimensions must be 8 mm in diameter and 6 mm in length, as mentioned before.

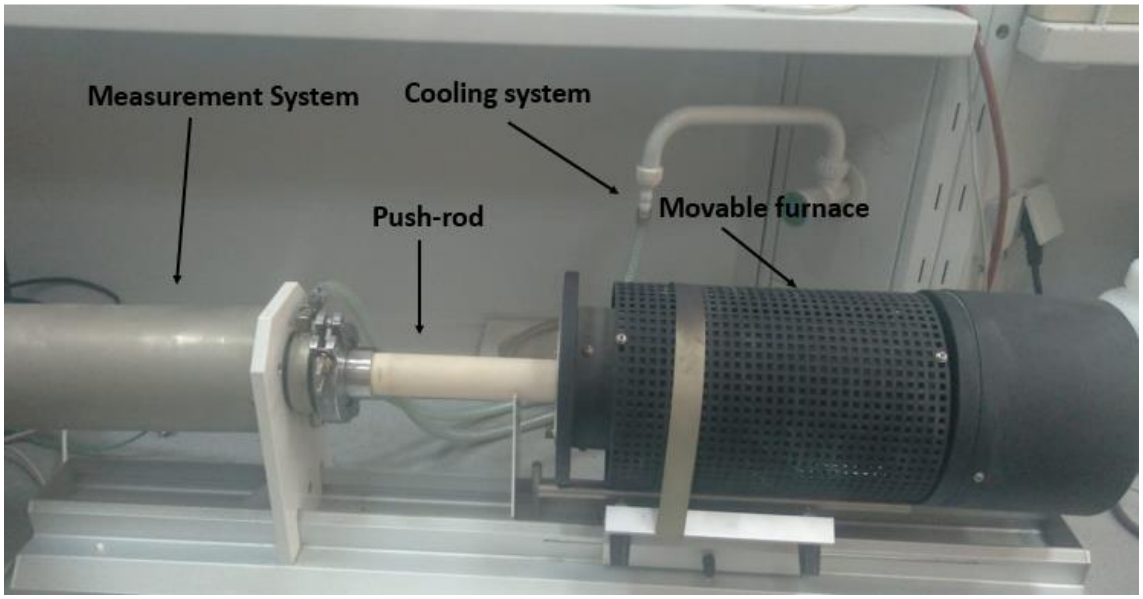

Figure 3.14. Demonstration of the horizontal dilatometer used to monitor pellets' sintering behaviour.

3.6. Density and Weight Measurements

Precisa precision balance and archimedean density kit were used for weight and density measurements in all experiments. It is shown in Figure 3.14. Archimedes' density measurement method measured the relative and bulk densities of the pellets.

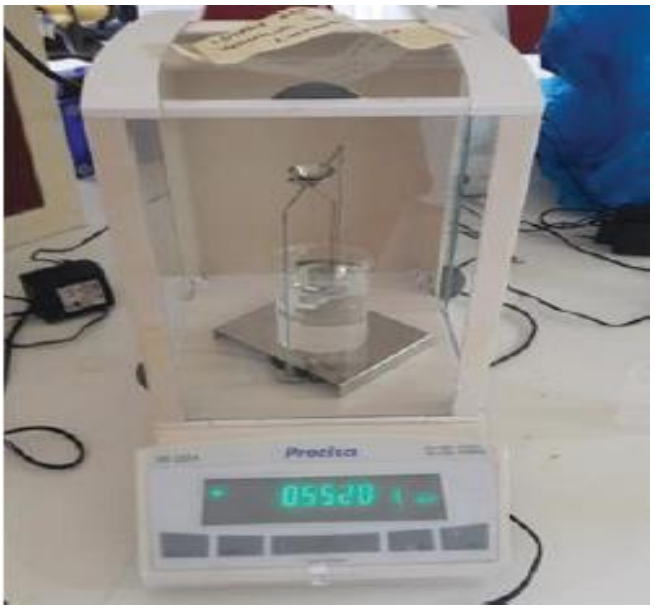

Figure 3.15. Archimedes' density measurement kit and precision balance.

The theoretical density of CT3000 LS SG Alumina powder was calculated as 3.93 g/cm^3 to calculate the relative density.

ASTM C373-88 standards were followed throughout Archimedes' density measurement experiments. First, the diameter, length, and weight data of all pellets are noted. The aim here is to calculate the geometric density of the cylindrical pellet and to check the accuracy of the bulk density data obtained by Archimedes' method. Then the dry weight measurements are taken. Dry weight is indicated by the abbreviation "D." If the samples are not taken from the kiln, they should be dried in an oven at 110 ^{0}C for 12 hours. The dry weight was noted for each sample, and the sample was placed in 40 ml of distilled water and allowed to boil for 2 hours. After boiling, the samples are allowed to cool to room temperature and are kept in distilled water for 12 hours. When this process is completed, the sample is placed on the lower balance of the Archimedes kit, which is immersed in the water-filled beaker, and the suspended weight is measured. Suspended weight is indicated by the abbreviation "S." After the suspended weight is noted, it is

wiped with a damp cloth to remove excess water on the pellet's surface. It is essential to adjust the humidity of the cloth well. If the cloth absorbs water from the open pores in the pellet, the measured relative and bulk density values will be wrong.

After removing excess water, the pellet is placed on the upper balance of the Archimedean density kit, and the saturated weight is measured. Saturated weight is indicated by the abbreviation "W." After noting the saturated weight value, the bulk density, and relative density values are found by substituting them in the formulas:

$$V=W-S \quad (3.1)$$

V-Exterior Volume

W-Saturated Weight

S-Suspended Weight

$$B=\frac{D}{V} \quad . \quad (3.2)$$

B-Bulk Density

D-Dry weight

V-Exterior Volume

Since the dry weight, suspended weight, and saturated weight information of the sample are noted, respectively, using these two formulas, the exterior volume and the bulk density can be easily calculated. The following formula is used to calculate the relative density values.

$$\%\text{Relative Density (\%RD)}=(\rho_{bulk}/\rho_{theoretical})*100 \quad (3.3)$$

Where ρ_{bulk} is the bulk density and is the $\rho_{theoretical}$ theoretical density. Finally, the geometric density of the cylindrical pellet and the measured bulk density values are compared. The steps followed in Archimedes' density measurement are given in Figure 3.15.

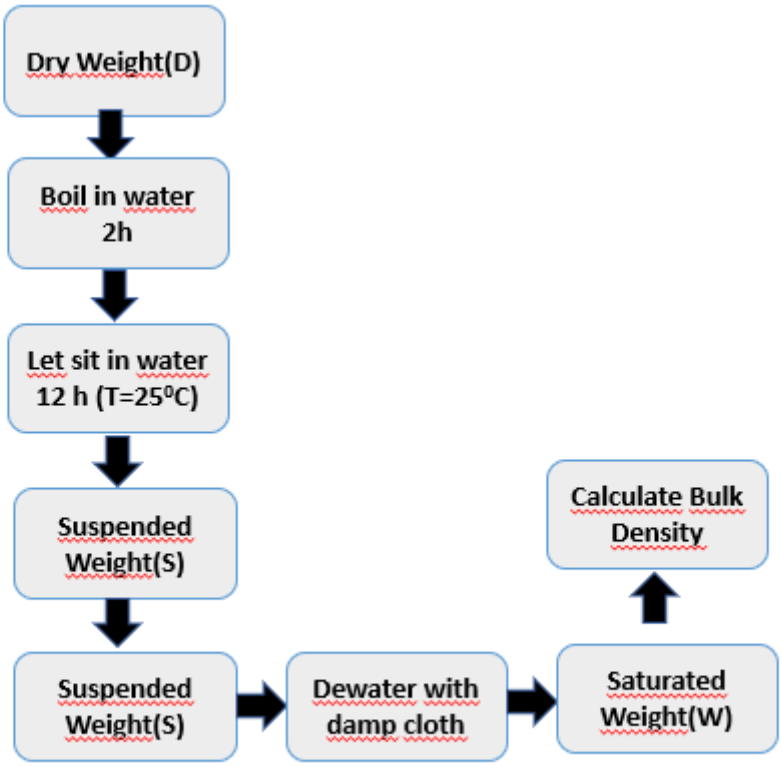

Figure 3.16. Experimental steps followed in Archimedes' density measurement

3.7. Characterization

While measuring the average particle size for the characterization of the powder, the average particle size was calculated using a laser scattering particle size distribution analyzer (HORIBA-LA960). The powder's particle size distribution was also plotted as a histogram with the same method. Specific surface areas of powders are measured by Brunauer, Emmet, and Teller (BET) (Micromeritics Gemini V). Particle morphologies of powders and fracture surfaces of the pellets were investigated using SEM (SEM, Philips XL-30S FEG). Also, Energy Dispersive X-ray (EDX) area analysis is done with SEM. The thermal behavior of the powders was investigated with a TGA/DTA (Perkin Elmer Diamond) simultaneous thermal analyzer. The powders were subjected to a gradual increase in temperature with a heating rate of 5 °C per minute until they reached 1200 °C. X-ray diffraction (XRD, Philips X-Pert Pro) examined the present crystalline phases. Search-match is made with Panalytical HighScore Plus software. The sintering behavior of the powders was investigated by dilatometric method. The powders were uniaxially pressed at 200 MPa (Φ:8 mm), and the compacts were sintered in the horizontal

dilatometer (Linseis L76150B-1600) up to 1300 and 1500 ^{0}C under static air with different heating rates of 1.1, 3.3 and 9.9 ^{0}C/min. Archimedes ' method measured the final densities of the sintered compacts (ASTM C373-88). The theoretical density for alumina was taken as 3.93 g/cm^{3}.To investigate the microstructure of the sintered compacts, specimens were cut from their center and then examined by SEM.

CHAPTER 4

RESULTS AND DISCUSSION

4.1. Powder Characterization

Commercially available CT3000 LS SG Alumina powder is the starting material, and its physical and chemical properties are given in Chapter-3. Particle size alone does not mean anything. Therefore, the surface area of the powder was measured first. The specific surface area (SSA) of the powders was measured by the BET method. And It is 8.53 m^2/g. Both published and measured SSA values of the powders are given in Table 4.1. Published data were obtained from the producer and may change from lot to lot. Measured SSA values differed slightly from the published value, as expected. The average grain size was measured using a laser scattering particle size distribution analyzer (HORIBA-LA960). And 0.56 μm was found. As expected, there is a slight difference between the estimated average particle size and the producer's data. The difference comes from a soft aggregation of primary particles.

Table 4.1. BET and Average Grain Size Measurements

	CT3000 LS SG Alumina
Measured specific surface area(m^2/g)	8.53
SSA (data from the producer)(m^2/g)	7.80
Measured average particle size (μm)	0.56
Published Average particle size (μm)	0.50

According to the data from the manufacturer, the D_{50} and D_{90} values of the powder are 0.5 and 2 μm, respectively. This gives information about the particle size distribution, but the D_{10} value is not given. To investigate the powder in more detail, the particle size distribution of the powder was examined using a laser scattering particle size distribution analyser (HORIBA-LA960). The particle size distribution graph of CT3000 LS SG powder is given in Figure 4.1.

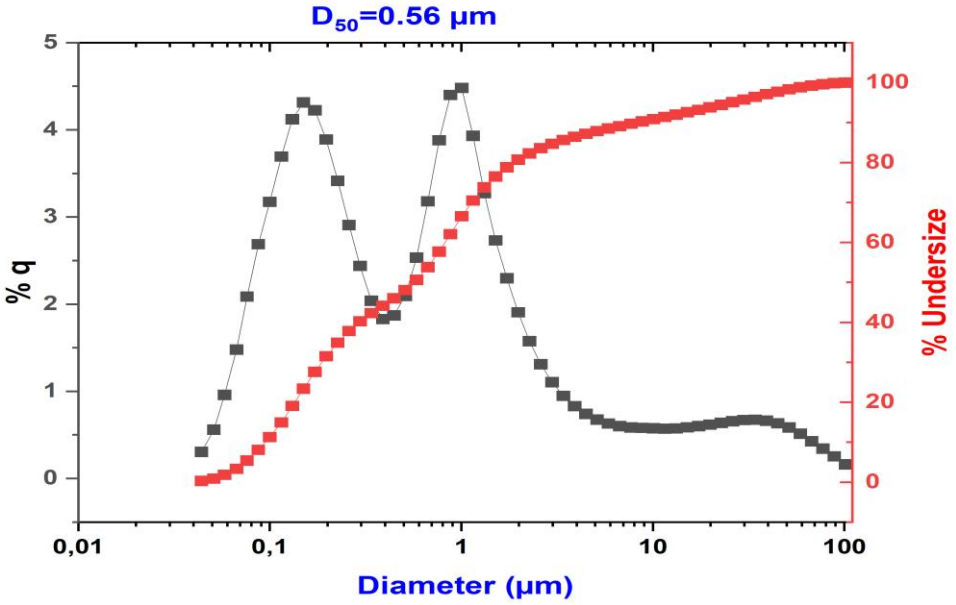

Figure 4.1. Particle size distribution of CT3000 LS SG Alumina powder.

Laser scattering particle size distribution graph, particle size ranges between 0.04 to 102 µm diameter. D_{50} is 0.56 µm, as denoted earlier. It is in good accordance with the data provided by the producer. In addition, the CT3000 LS SG powder is bimodal. Powder characteristics are playing important role in ceramic processing. The final properties of the ceramic parts depend on the particle size, particle shape, particle size distribution, surface area and purity. Particle size and surface area affects the reactivity of the powder and the mechanical properties of the final product.

On the other hand, particle size 54trength54ion determines the packing density and green 54trength of the ceramic compact. Particle size, shape and distribution influence the sintering behaviour of the powder. Powder characteristics influence how well particles pack together during sintering, which in turn affects the density, strength, and porosity of the final ceramic product.

In conclusion, powder characteristics are fundamental in ceramic processing because they influence the entire production cycle, from powder preparation to sintering and final product quality. Controlling these characteristics is essential for achieving the desired properties, performance, and consistency in ceramic materials. Also, particle morphology is important.The SEM secondary electron images of the powder are given below in Figure 4.2.

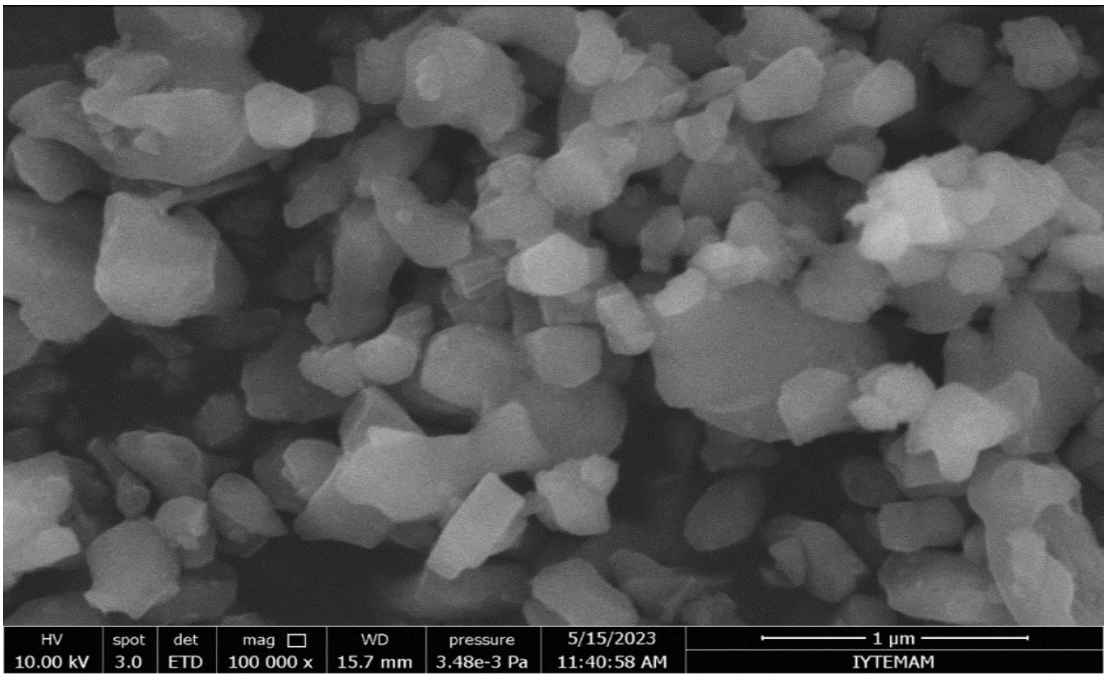

Figure 4.2. SEM Secondary Electron Image of the untreated CT3000 LS SG Alumina powder.

As denoted earlier, powder morphology is important. The morphology of ceramic powders significantly affects their sintering behavior. Particles with different shapes and sizes can pack differently during sintering. Properly controlled powder morphology can result in improved particle packing, leading to higher densities and enhanced sintering kinetics, which ultimately affect the strength and properties of the final ceramic product. In Figure 4.2., it can be seen that there are some agglomerations in the micrograph. These agglomerations can lead to poor green compaction, reduced sintering uniformity and density variations. To overcome these issues caused by powder agglomeration, ceramic manufacturers often employ various strategies, including de-agglomeration processes such as milling.

Figure 4.3. shows the XRD results of the CT3000 LS SG Alumina powder.XRD pattern matches with the JCPDS number 00-042-1468.

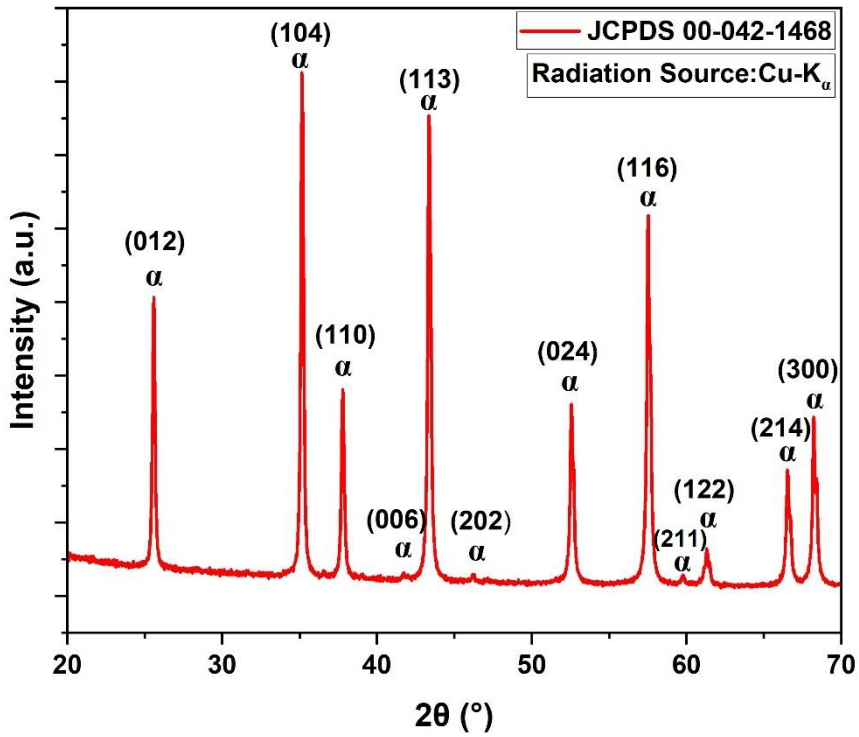

Figure 4.3. XRD pattern of CT3000 LS SG Alumina powder.

The main phase is α-Al_2O_3, and the its crystal structure has hexagonal symmetry with space group $R\bar{3}c$. The peaks for the alpha phase were quite clear. As described in Chapter-2 and Chapter-3, the infiltration solution was a polymeric precursor containing Al^{+3} ions. The thesis aims to infiltrate the polymeric solution containing Al^{+3} ions into the porous scaffold, after which the volatile substances in the solution are removed at 400 ^{0}C, and the oxide nanoparticles are precipitated into the pores. Due to their small grain sizes and high surface areas, these precipitated nanoparticles are expected to increase the densification rate by entering the reaction earlier at sintering temperatures. Therefore, the solution containing Al^{+3} ions was dried in an oven at 250 ^{0}C for 3 hours and a powder. For investigating the presence of oxide nanoparticles at sintering temperatures, it is essential to characterize this powder(called E-powder).

The specific surface area (SSA) of this powder was measured by the BET method. And It is 8.93 m^2/g. The average grain size was calculated using a laser scattering particle

size distribution analyser (HORIBA-LA960). And 0.136 μm was found. The SEM image of the powder is given in Figure 4.4.

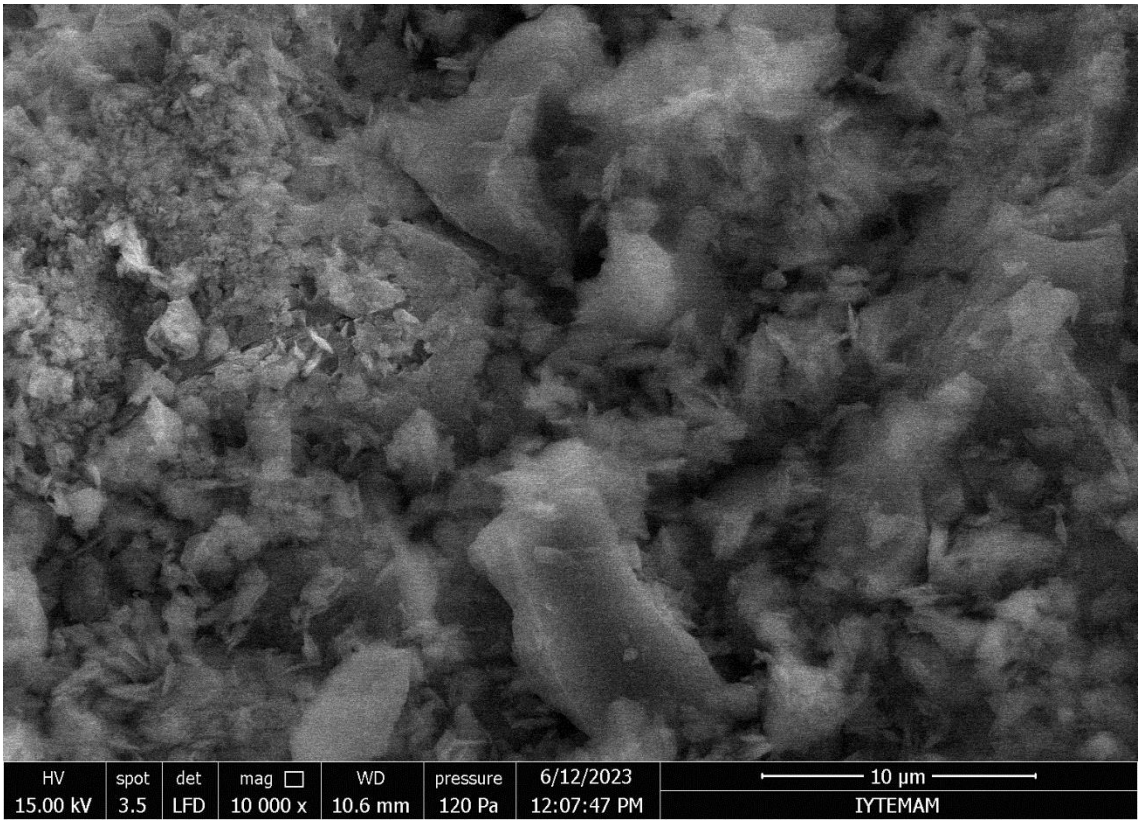

Figure 4.4. SEM secondary electron image of the E-powder.

As expected, obtaining secondary electron images of the E-powder by SEM was challenging. Although the E-powder was coated with gold, the image resolution was affected due to the charging effect and local melting of polymers due to the accelerated electron beam. However, the untreated E-powder morphologically appears to be composed of amorphous polymeric parts. The XRD pattern of the E-powder is shown in Figure 4.5. For the E-powder, x-rays will be scattered in many directions leading to a bump distributed in a wide range instead of high-intensity narrower peaks because of the non-crystalline nature of the polymers. The morphological structure of the untreated E-powder was examined by SEM and confirmed by XRD that the powder was covered with amorphous polymeric portions.

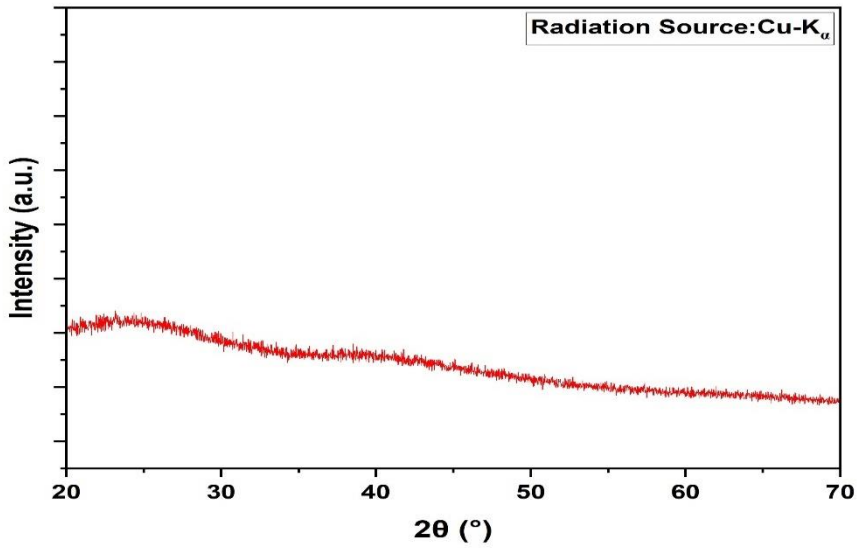

Figure 4.5. XRD pattern of the E-powder

At that point, the thermal behavior of the E-powder is investigated with TGA/DTA simultaneous thermal analyzer. Thermal curve of the E-powder is given in Figure 4.6.

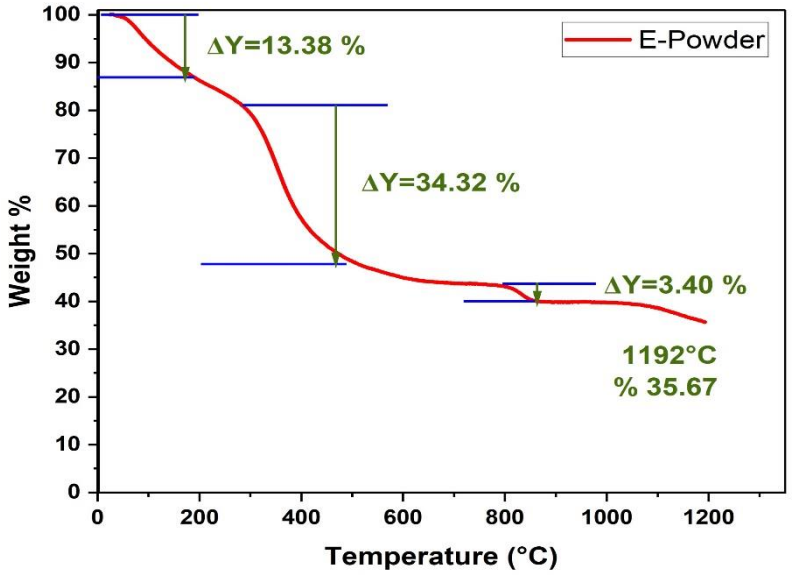

Figure 4.6. TGA graph of E-powder

E-powder is heated up to 1200 ^{0}C with a heating rate of 5 ^{0}/min. When the graph is examined, an initial weight loss of 13.38 % is seen in the temperature range of approximately 25 to 200 ^{o}C. Second weight loss, of 34.32 %, occurs between 300-500 ^{o}C. Third, weight loss takes place between 800-850 ^{o}C. That is the lowest recorded weight loss reaching 3.40 %. Final weight loss occurs at 1192 ^{0}C with 35.67 %. Note that this is the highest weight loss. In all these temperature ranges, it can be thought that the polymers formed by the polymerization of ethylene glycol,2-butoxy ethanol, deionized water, and aluminum salts are removed from the structure. In light of the information given by the TGA analysis, the E-powder was subjected to heat treatment. The E- powder was heat treated in a furnace with a soaking time of 1 hour at 300, 500, 700, 900, 1100, and 1300 ^{0}C, respectively. XRD results are given in Figure 4.7.

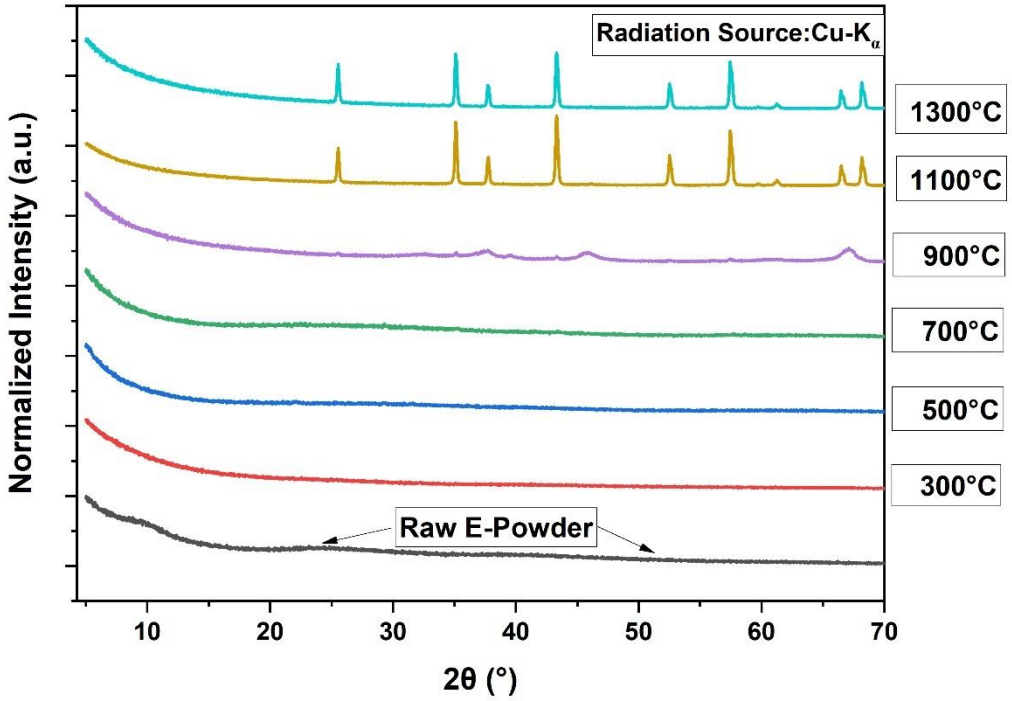

Figure 4.7. XRD results of the untreated and heat-treated E-powder. Heat treatment temperatures are 300,500,700,900,1100 and 1300 ^{0}C. Soaking time is 1 hour.

As can be seen from the graph above, powders heat treated at 300, 500, and 700 ^{0}C have the same amorphous character as the untreated sample. Therefore, the bump appears again due to amorphous phases. However, the peaks at 900 ^{o}C indicate that the crystalline phase has formed. When it comes to powders heat treated at 1100 and 1300

^{o}C, the peaks of the crystalline phase become more pronounced. The XRD results of the E-powder heat treated at 1100 and 1300 ^{0}C are given in Figures 4.8,4.9, respectively.

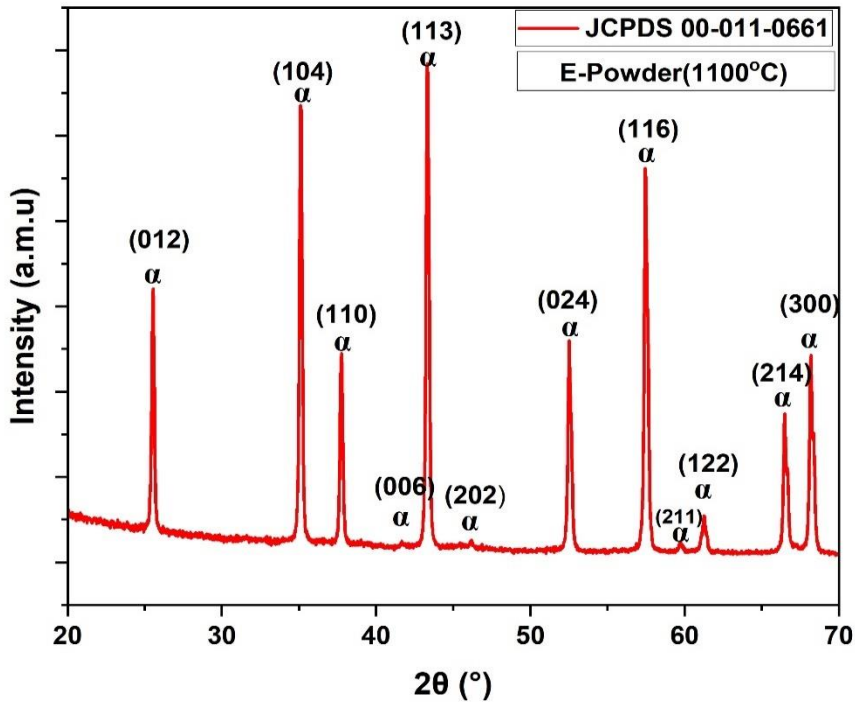

Figure 4.8. XRD pattern of the E-powder heat treated at 1100 ^{o}C and soaking time is 1 hour.

At 1100 ^{0}C, the number of peaks that belong to a crystalline phase increases with crystallization. After the search-match application, The XRD pattern of E-powder heat treated at 1100 ^{0}C fully matches the JCPDS 00-011-0661 card. The investigated crystalline phase is again α-Al_2O_3 and ıts crystal structure as like CT3000 LS SG Alumina powder has hexagonal symmetry with space group $R\bar{3}c$. As expected, this result showed the presence of α-Alumina nanoparticles at the sintering temperatures. The lattice parameters are the difference between the JCPDS card of 00-042-1468 and the JCPDS card of 00-011-0661. The Scherrer equation can calculate the size of the crystallized nanoparticles:

$$D = \frac{K\lambda}{\beta \cos\theta} \quad (4.1)$$

Where,

D:Crystallite size(nm)

K:Scherrer constant(0.94)

λ:Wavelength of the x-ray sources(0.15406 nm)

β:Full-Width at Half Maximum (radians)

θ:Peak position(radians)

With the help of X'Pert HighScore Plus software, the FWHM of the most intense peak is determined; its value is 0.133(radians), and its peak position is 43.3 ^{0}. The size of the nanoparticles formed at 1100 ^{0}C in the presence of this information is 71 nm.

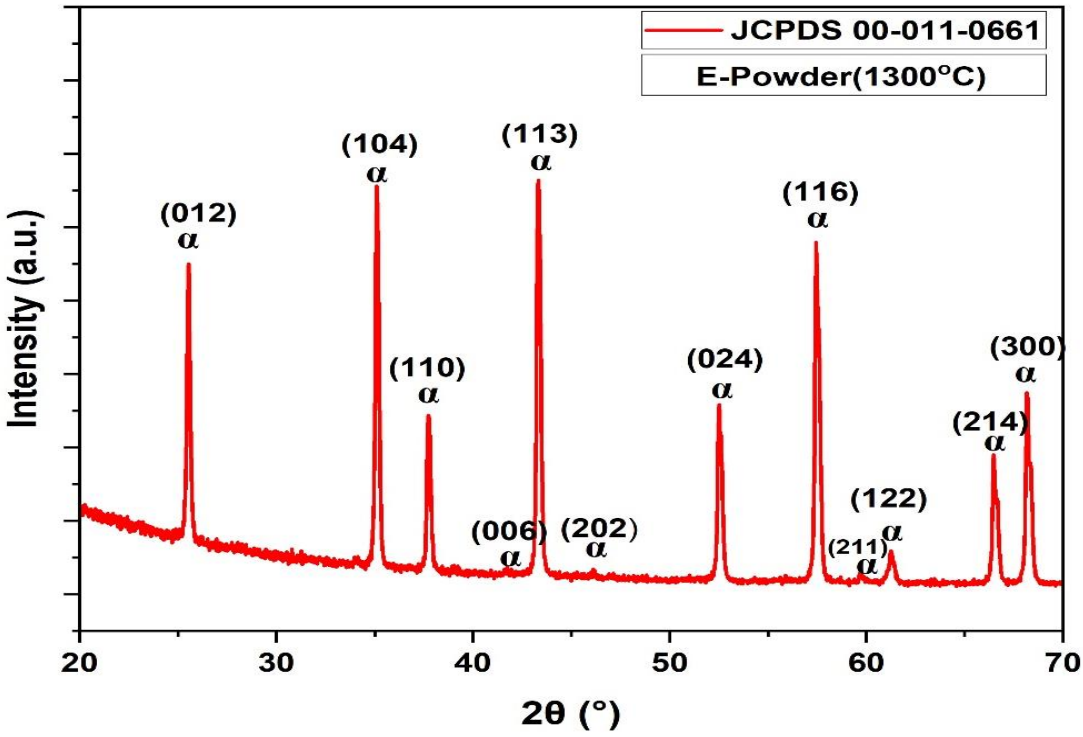

Figure 4.9. XRD pattern of the E-powder heat treated at 1300 ^{o}C and soaking time is 1 hour.

E-powder heat-treated at 1300 ^{o}C has the same JCPDS number as E-powder at 1100 ^{o}C .This crystalline phase is α-Al_2O_3, and its crystal structure Alumina powder has hexagonal symmetry with space group $R\bar{3}c$. Again with the help of X'Pert High Score Plus, the FWHM value of the highest intensity peak was found to be 0.117(radians), and

the peak position was 43.3 º. As expected, the size of the calculated nanoparticles increased to 82 nm at higher temperatures. To support the XRD data, changes in the material structure with heat treatment were observed with SEM secondary electron images. At 300 ºC, the presence of polymeric residues can be seen in Figure 4.10. The XRD results agree with what appears in the SEM secondary electron image. Amorphous polymeric parts appear as bumps in the XRD pattern, and morphologically entangled polymeric components appear in SEM.

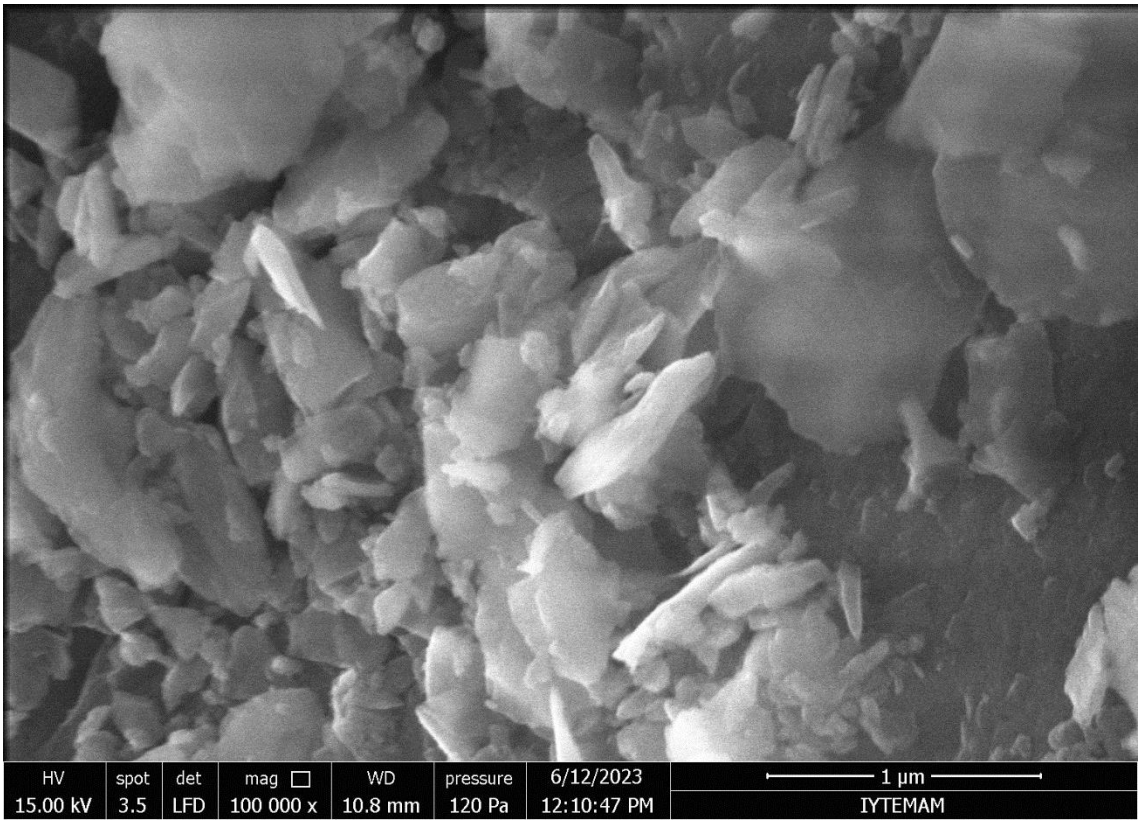

Figure 4.10. SEM secondary electron images of the E-powder heat treated at 300 ^{0}C. The soaking time is 1 hour.

At 500 ºC, It is thought that the polymeric parts melt, but their residues persist in the structure. The particles are believed to still be coated with polymeric residues, and these non-conductive polymeric residues are thought to impede imaging. So, the non-conductive polymeric part leads to the charging effect. The charging effect refers to the accumulation of electrical charge on the surface of a specimen when bombarded by an electron beam. This phenomenon occurs because the high-energy electrons in the beam can dislodge or excite electrons from atoms in the sample material, causing them to

become positively charged. As a result, an imbalance of charges occurs, leading to the buildup of static electricity on the specimen's surface.

The SEM secondary image of the E-powder that is heat treated at 500 ^{o}C with a soaking time of 1 hour is presented in Figure 4.11.

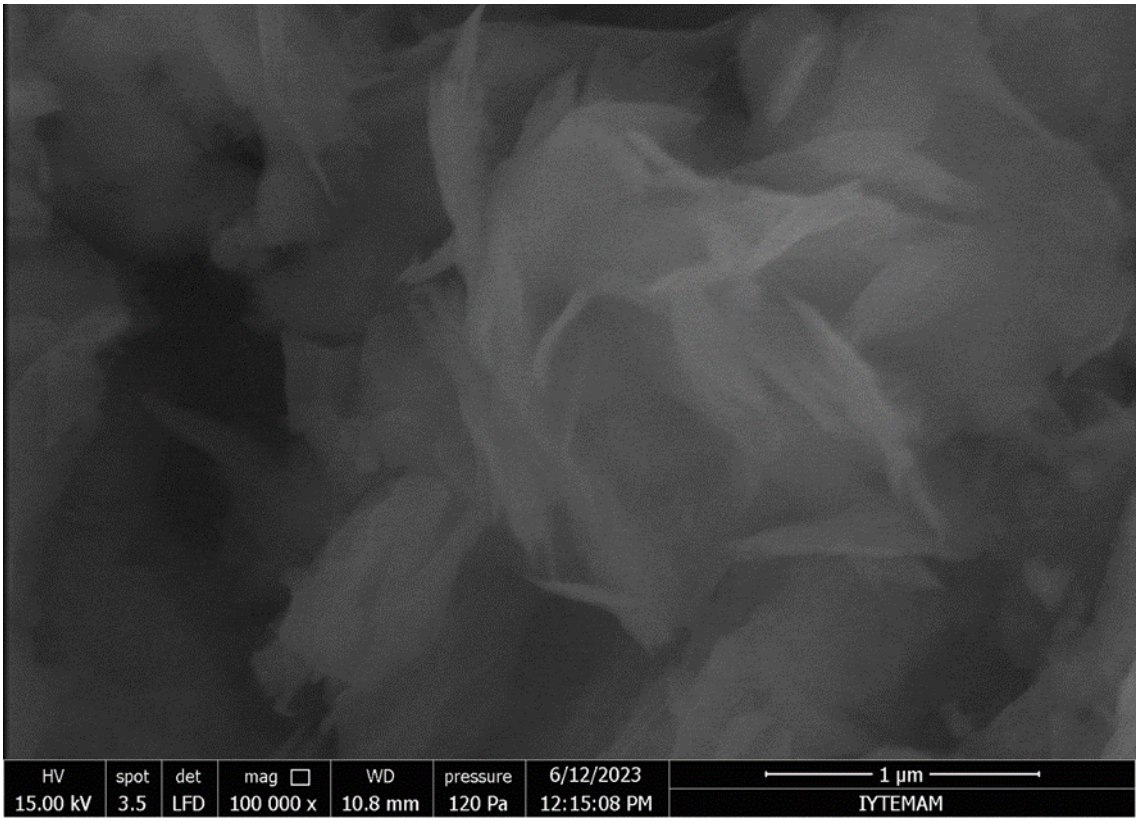

Figure 4.11. SEM secondary electron images of the heat-treated E-powder at 500 ^{0}C. The soaking time is 1 hour.

Especially at these temperatures, although the samples were covered with gold, the charging effect made it difficult to take images because the polymers are insulators. The SEM secondary image of the E-powder that is heat treated at 500 ^{o}C with a soaking time of 1 hour is presented in Figure 4.11.

Even if particles are present, it is likely that at these temperatures, their surface is covered with burnt polymer residues. When it comes to 700 ^{o}C, the burned polymeric parts also start moving away from the structure slowly due to the increasing temperature. The SEM secondary image of the E-powder that is heat treated at 700 ^{o}C with a soaking time of 1 hour is presented in Figure 4.12.

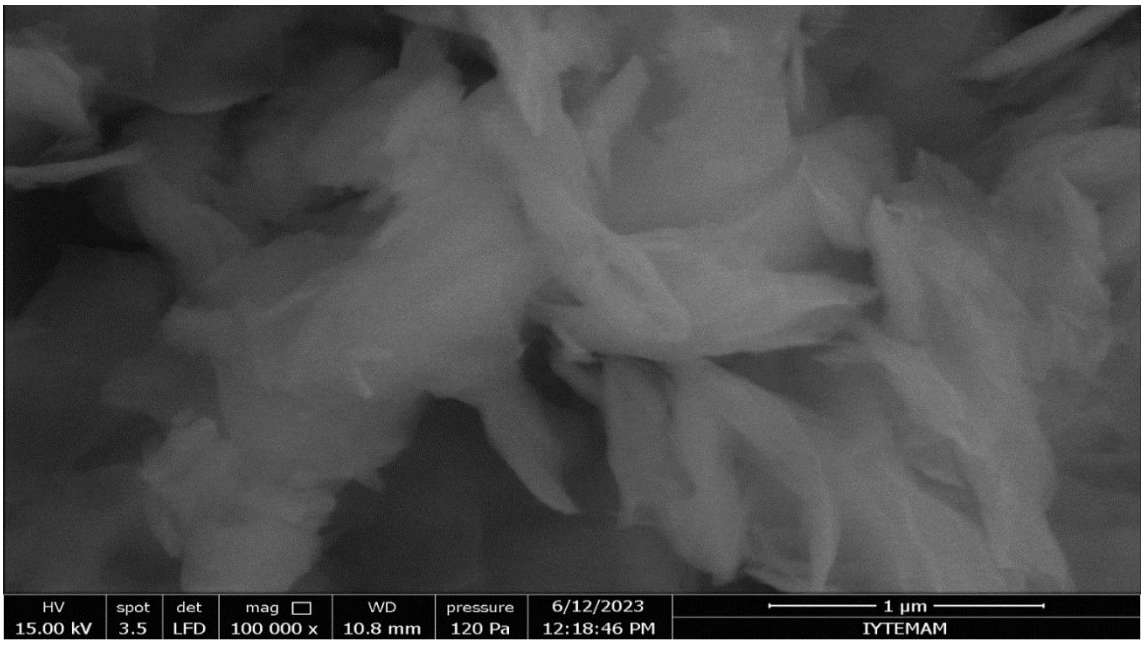

Figure 4.12. SEM secondary electron images of the E-powder heat treated at 700 ^{0}C.The soaking time is 1 hour.

In an X-ray diffraction (XRD) pattern, the crystallization of an amorphous material with temperature refers to the transformation of the material's structural arrangement into a regular crystal structure due to the influence of heat. This signifies the transition of an amorphous material to a regular crystalline phase with increasing temperature.

Amorphous materials are substances in which atoms do not have a regular crystal structure. Therefore, an XRD analysis of an amorphous material typically does not reveal a crystallization pattern because the atoms are distributed irregularly. However, at a sufficiently high temperature or under the influence of another activating factor, an amorphous material can transition into a regular crystal structure. A few peaks that belong to a crystal phase are seen in the XRD pattern at 900 ^{o}C, but SEM investigation shows no sign of the presence of nanoparticles.

The SEM secondary image of the E-powder that is heat treated at 900 ^{o}C with a soaking time of 1 hour is shown in Figure 4.13.

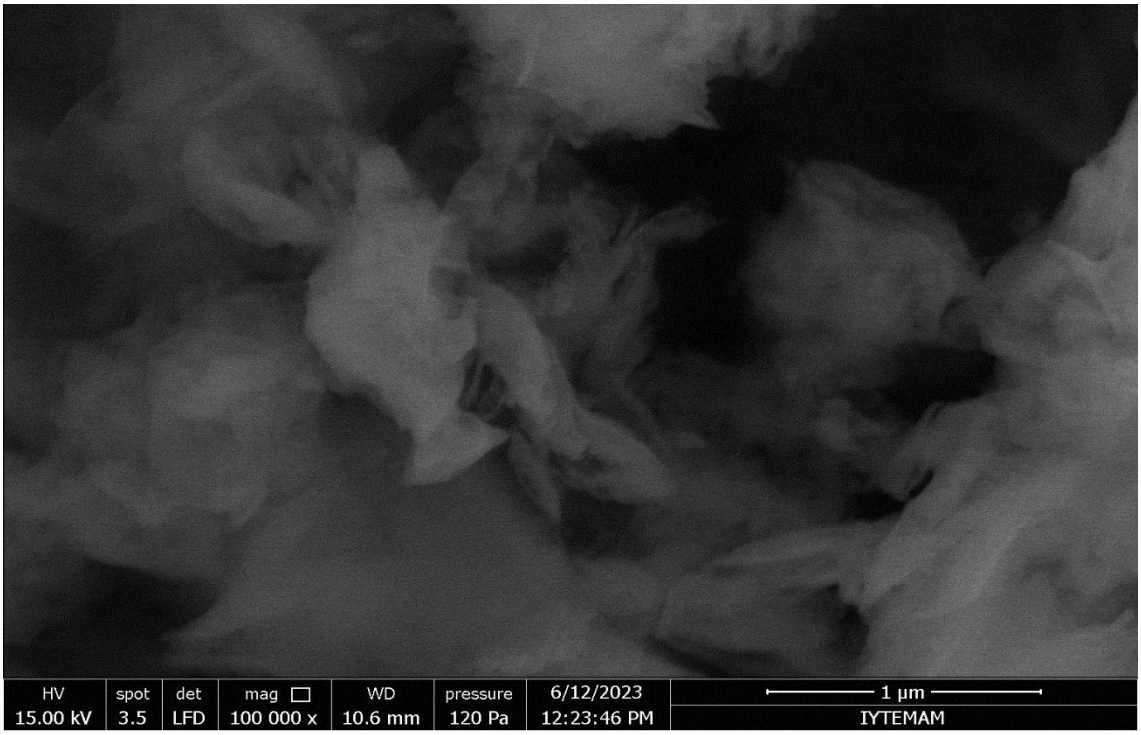

Figure 4.13. SEM secondary electron images of the E-powder that is heat treated at 900 ^{0}C.The soaking time is 1 hour.

It has been observed that when the temperature reaches 1100°C, nanoparticles start to form. During X-ray diffraction (XRD) analysis, an excellent correlation was found with the peaks corresponding to the crystal phase, specifically α-Alumina. Furthermore, the crystallite size was determined to be 71 nanometers. This was further substantiated by scanning electron microscopy (SEM) secondary electron images, which clearly indicate the presence of nanoparticles with dimensions matching the calculated size. For certain applications, it is of paramount importance that these crystallized nanoparticles exhibit an identical crystal structure to that of the CT 3000 LS SG Alumina powder, ensuring that they do not introduce any discernible variations in electrical or thermodynamic properties upon precipitation into the material's structure. This requirement underscores the significance of maintaining the material's intrinsic characteristics and performance attributes, while harnessing the benefits conferred by the presence of the nanoparticles.

This congruence in crystal structure between the newly formed nanoparticles and the CT 3000 LS SG Alumina powder serves as a fundamental prerequisite for seamless

integration into the host material. It not only guarantees the preservation of electrical and thermodynamic properties but also reinforces the material's overall structural integrity. The remarkable consistency in crystal structure not only enhances the material's electrical conductivity but also bolsters its thermodynamic stability. This has far-reaching implications for applications where precise control over electrical and thermal behavior is critical.

Figure 4.14. illustrates the SEM secondary image of the E-powder, which underwent heat treatment at 1100°C for a duration of 1 hour.

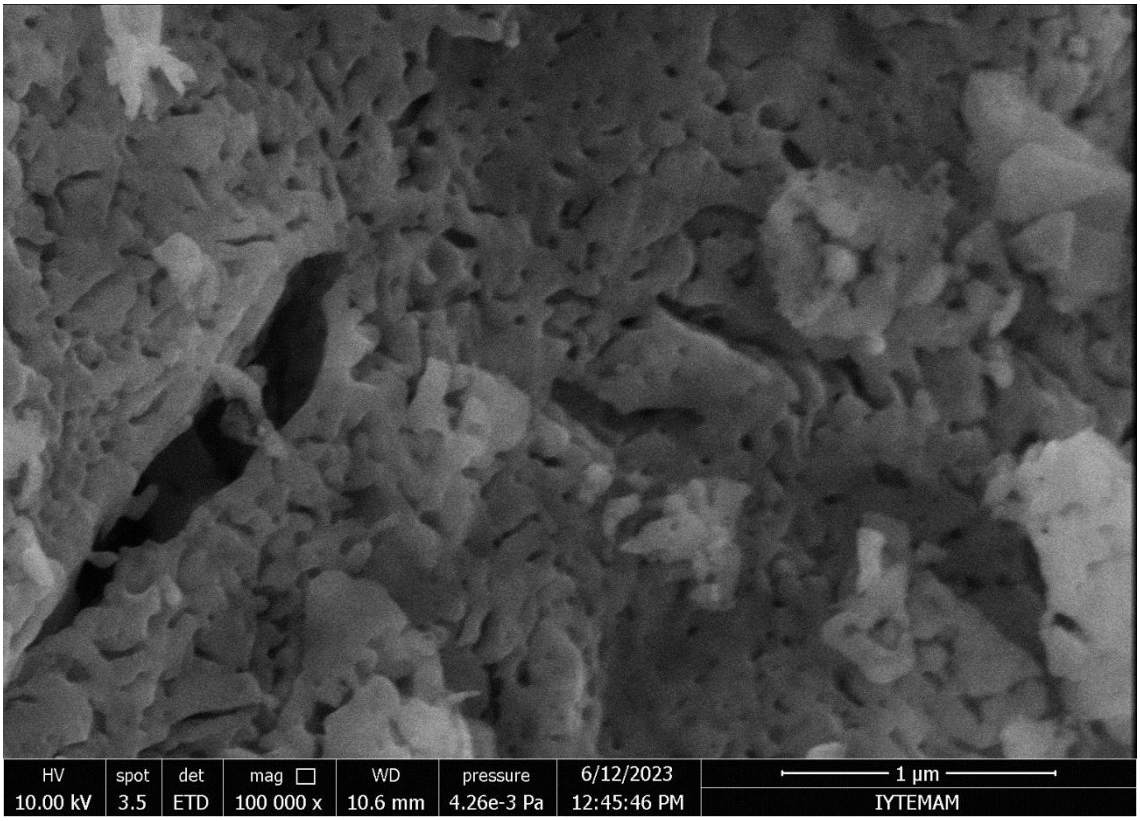

Figure 4.14. The SEM secondary image of the E-powder heat treated at 1100 ^{o}C with a soaking time of 1 hour.

At 1300 ^{o}C, these nanoparticles grew with the effect of temperature, and the average crystallite size increased to 80.1 nm. In the XRD data, the peaks became more pronounced at 1300 ^{o}C than at 900 and 1100 ^{0}C, and particles can be easily distinguished in SEM investigation. The SEM secondary image of the E-powder that is heat treated at 1300 ^{o}C with a soaking time of 1 hour is shown in Figure 4.15.

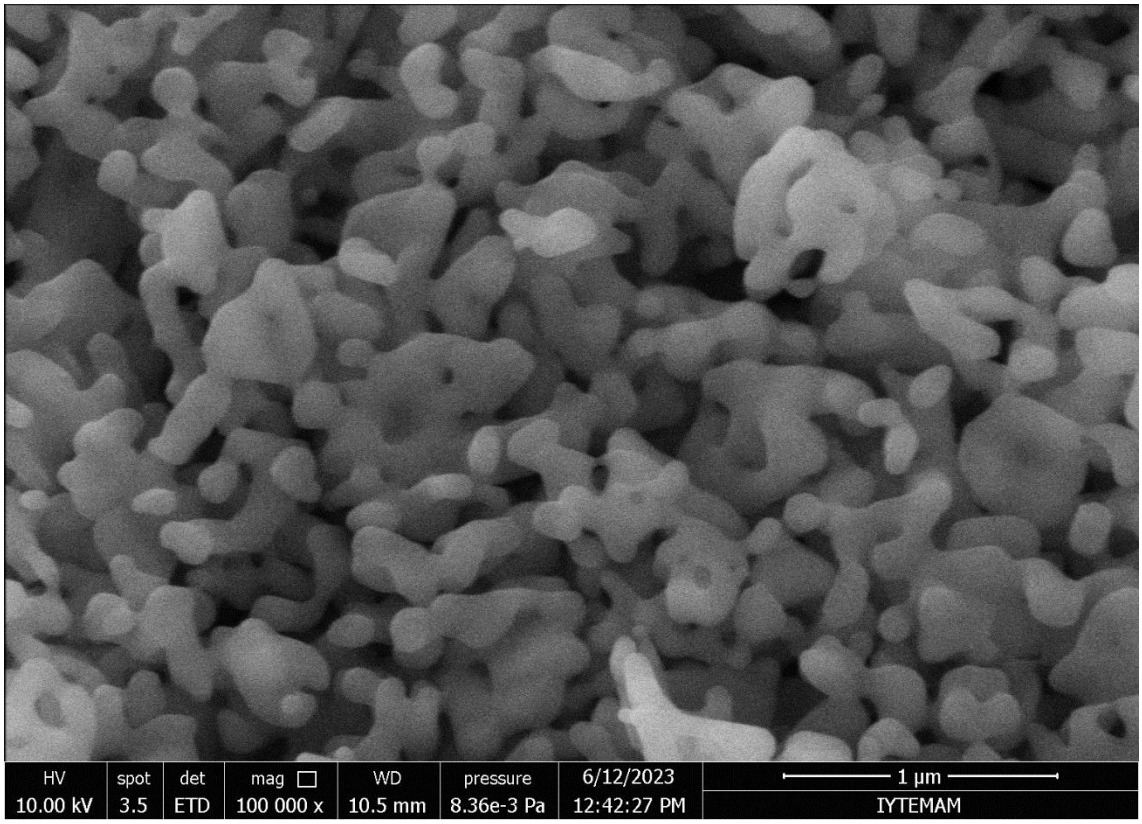

Figure 4.15. The SEM secondary image of the E-powder heat treated at 1300 ^{o}C with a soaking time of 1 hour.

The existence of nanoparticles at 1300 ^{0}C has been proven by analyzing SEM secondary electron images and XRD patterns. And the average crystallite size calculated by Scherrer's equation at 1300 ^{0}C is 81 nm. This shows the fineness of the nanoparticles. So, their surface area is very high. They are very reactive at sintering temperatures, as expected in the study.

4.2. Characterization of the Bisque-Fired Pellets

As mentioned in the experimental part, before the infiltrated samples were prepared, CT3000 LS SG Alumina powder was turned into pellets with a uniaxial press at 200 Mpa pressure. This prepared pellet was pre-heated at 1100 ^{0}C. This heat treatment is called "bisque firing." The purpose of bisque firing was to facilitate the pellets' handling and prevent dispersal by ensuring that the pellet had a particular strength during

the infiltration process. At the same time, pores are formed in the structure of this pellet at 1100 ^{o}C, and it is expected to host the solution to be infiltrated. This heat-treated porous structure(or porous pellet) is called a "scaffold." The bulk densities of Alumina scaffolds were measured by Archimedes' principle. And their relative densities vary between 50 and 60 %. Theoretical density of CT3000 LS SG Alumina is taken as 3.93 g/cm^3 from the published data. Therefore, they contain 40-50 % porosity. SEM secondary electron images of the fracture surface of these pellets are shown in Figure 4.16.

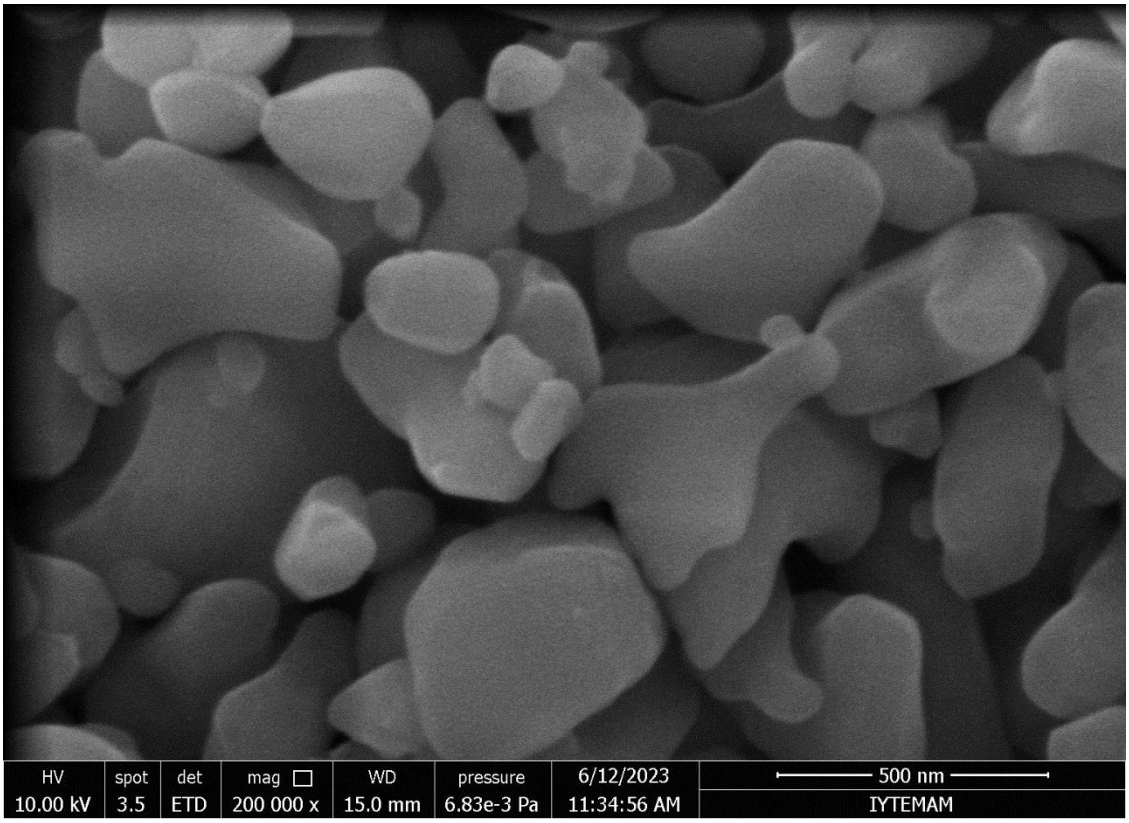

Figure 4.16. SEM secondary electron image of the fracture surface of the bisque-fired pellets at 1100 ^{0}C.

The SEM images showed that the microstructure contains many pores, which is why it is called a scaffold. Thus, following the purpose of the study, the air in the pores can be removed utilizing the vacuum pump, and the infiltration solution can be placed in these pores. The bisque-fired pellet contains narrow pore channels (0.1 to 1 μm), and these pores are effective in the capillary action of the polymer precursor solution.

4.3. Coding of the Samples

As mentioned in the experimental stage, there are three groups of samples: reference, infiltrated, and pellets obtained from loose CT3000 LS SG Alumina powder washed with polymer precursor solution. The first group is infiltrated samples. Infiltrated samples are named "AK" if they are sintered in a laboratory kiln and "AD" if they are sintered in a dilatometer. Second group is the pellet formed by polymer precursor solution coated loose powder. These samples are coded with the letter "P." The third group samples are non-infiltrated reference pellets. These samples are coded with the letter "R."

4.4. Density Measurements

In the first stage, furnace experiments were designed for the three groups of pellets mentioned above, and the relative density values were monitored. Then, dilatometer experiments were created by looking at the trends in relative densities. The theoretical density of Alumina is taken as 3.93 g/cm^3.

Archimedes' density measurements of the reference pellets are given in Table 4.2. for furnace experiments.

Table 4.2. Archimedes' Density Results of the Reference Pellets

Code of Sample	**Sintering Temperature(^{o}C)**	**Heating Rate(^{0}/min.)**	**%Relative Density**
R1	1300	3.3	68.2
R2	1300	6.6	66.1
R3	1300	9.9	65.3
R4	1500	3.3	90.7
R5	1500	6.6	87.8
R6	1500	9.9	86.7

The density measurements of the infiltrated pellets, as determined through Archimedes' method, are provided in Table 4.3.

Table 4.3. Archimedes' Density Results of Infiltrated Pellets

Code of Sample	Sintering Temperature(°C)	Heating Rate(^{0}/min.)	%Relative Density
AK-1(5x)	1300	3.3	69.0 (+1.2 %)
AK-2(5x)	1300	6.6	66.7 (+0.9 %)
AK-3(5x)	1300	9.9	65.9 (+0.9 %)
AK-4(15x)	1300	3.3	71.3 (+1.6 %)
AK-5(15x)	1300	6.6	68.3 (+3.3 %)
AK-6(15x)	1300	9.9	66.9 (+1.6 %)
AK-7(5x)	1500	3.3	91.2 (+2.5 %)
AK-8(5x)	1500	6.6	89.2 (+1.6 %)
AK-9(5x)	1500	9.9	87.7 (+1.2 %)
AK-10(15x)	1500	3.3	92.5 (+2.0 %)
AK-11(15x)	1500	6.6	89.8 (+2.3 %)
AK-12(15x)	1500	9.9	87.8 (+1.3 %)

*Soaking time is 1 hour. All the pellets are bisque fired at 1100 ^{0}C.

Finally, Archimedes' relative density values of the pellets produced by the uniaxial press with 200 Mpa pressure of the powder obtained by drying the loose powder washed with polymer precursor solution are given in Table 4.4.

Table 4.4. Archimedes' density results of "p" pellets

Code of Sample	Sintering Temperature(°C)	Heating Rate(^{0}/min.)	%Relative Density
P1	1300	3.3	67.5 (-1.0 %)
P2	1300	6.6	65.9 (-0.3 %)
P3	1300	9.9	65.4 (+0.2 %)
P4	1500	3.3	90.8 (-3.4 %)
P5	1500	6.6	87.8 (0.0 %)
P6	1500	9.9	86.1 (-0.7 %)

The relative density values given in the tables will be examined with graphics. However, if it is generally deduced, the density increase was observed in the infiltrated samples compared to the reference samples. In contrast, the relative density values in the pellets produced with loose powder washed with polymer solution remained below the relative density values of the reference sample. This shows that post-loading nanoparticles into bisque-fired pellets give better results. Figure 4.17. presents the relative density changes in the reference samples.

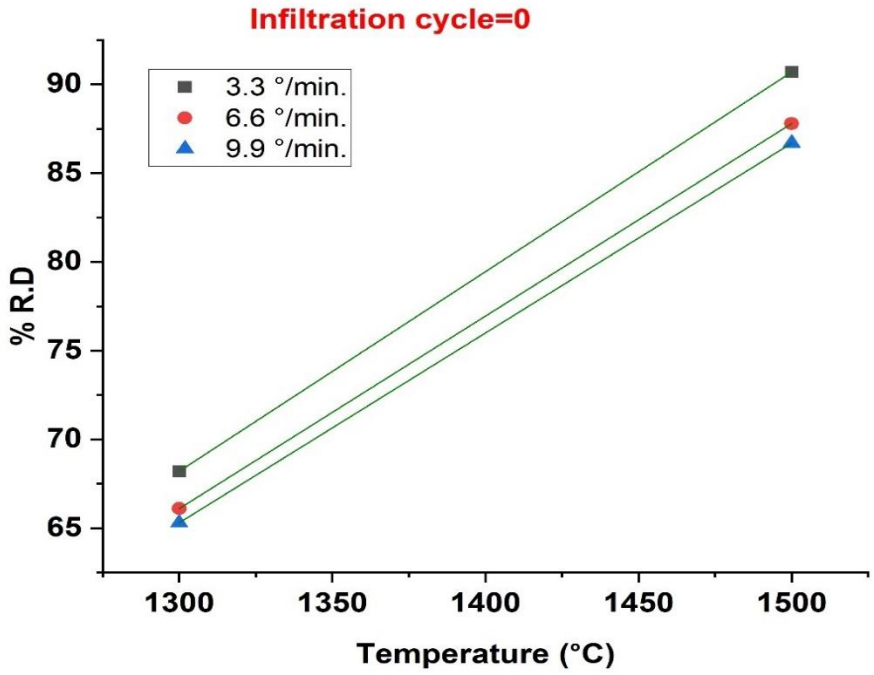

Figure 4.17. Changes in relative density values of the reference samples.

As expected in the graph, it is observed that the line shifts upwards as the heating rate decreases. High heating rates result in nonuniform microstructure and asymmetrical sintered neck forms due to unstable and nonuniform mass transfer, whereas in low heating rates, a uniform microstructure is obtained. Because of this, a higher final density can be attained with decreasing heating rates. At 1300 ^{o}C, the relative density values increased from 65.3 % to 68.2 % (+4.4 %) as the heating rate fell from 9.9 to 3.3 ^{0}C/min. . At 1500 ^{o}C, the relative density values increased from 86.7 % to 90.7 % (+4.6 %) as the heating rate decreased from 9.9 to 3.3 ^{0}C/min. . In light of these data, it is seen that the densification increases with temperature. This is because the temperature provides the necessary activation energy for diffusion. Since sintering is a diffusion-controlled process, the closer it is to the sintering temperature, the more activation energy is provided and the better the densification. Reference samples will be the main criterion for comparison with other samples.

The relative density changes of the 5x infiltrated samples are given in Figure 4.18.

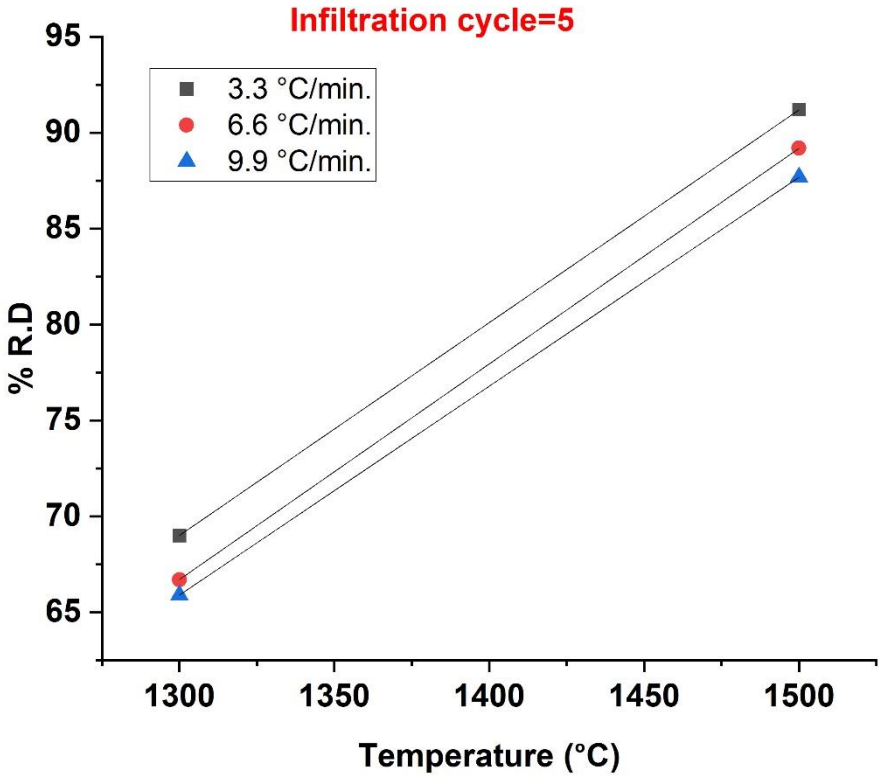

Figure 4.18. Changes in relative density values of the 5x infiltrated samples

Relative density trends in this graph are similar to reference samples. As the heating rate decreases, the lines in the graph shift upwards, and as the temperature increases, the densification increases. At 1300 ^{o}C, the relative density values increased from 65.9 % to 69 % (+4.7 %) as the heating rate decreased from 9.9 to 3.3 ^{0}C/min. . At 1500 ^{o}C, the relative density values increased from 87.7 % to 91.2 % (+3.9 %) as the heating rate fell from 9.9 to 3.3 ^{0}C/min. . Figures 4.17 and 4.18 differ because the relative density values increase slightly more than the reference samples due to nanoparticles in the 5x infiltrated samples.

These nanoparticles were expected to be active earlier than other particles due to the small particle sizes and high surface areas at these sintering temperatures, and they would form a neck between the particles. And when the graphs and tables are analyzed, at 1300 ^{0}C, an increase in relative density concerning reference samples of 1.2 % for the 3.3 ^{0}C/min., 0.9 % for the 6.6 ^{0}C/min. and 0.9 % for the 9.9 ^{0}C/min. are observed. At 1500 ^{0}C, an increase in relative density concerning reference samples of 2.5 % for the 3.3 ^{0}C/min., 1.6 % for the 6.6 ^{0}C/min. and 1.2 % for the 9.9 ^{0}C/min. are observed. When the

temperature increased from 1300 to 1500 ^{0}C, the highest relative density increase for reference samples was 2.5 % at 1500 ^{o}C with a heating rate of 3.3 ^{o}C/min. These results show that the nanoparticles reach their goal, but the infiltration load should be increased even more.

The relative density changes of the 15x infiltrated samples are given in Figure 4.19.

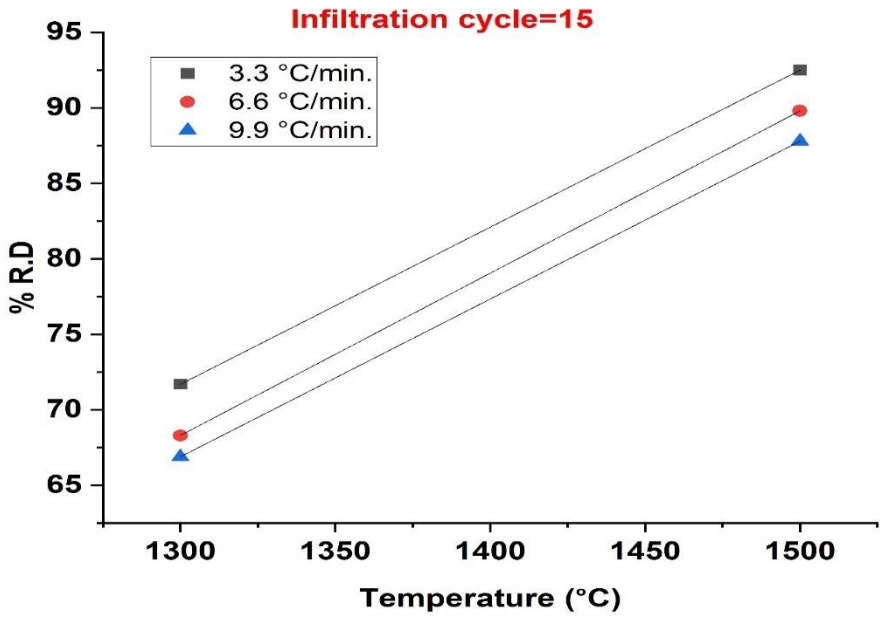

Figure 4.19. Changes in relative density values of the 15x infiltrated samples

Relative density trends in this graph are parallel to the reference and 5x infiltrated samples. As the heating rate decreases, the lines in the graph shift upwards, and as the temperature increases, the densification increases. At 1300 ^{o}C, the relative density values increased from 66.9 % to 71.3 % (+6.6 %) as the heating rate decreased from 9.9 to 3.3 ^{0}C/min. . At 1500 ^{o}C, the relative density values increased from 87.8 % to 92.5 % (+5.4 %) as the heating rate fell from 9.9 to 3.3 ^{0}C/min. . At 1300 ^{0}C, an increase in relative density concerning reference samples of 1.6 % for the 3.3 ^{0}C/min., 3.3 % for the 6.6 ^{0}C/min. and 1.6 % for the 9.9 ^{0}C/min. are observed. At 1500 ^{0}C, an increase in relative density concerning reference samples of 2.0 % for the 3.3 ^{0}C/min., 2.3 % for the 6.6 ^{0}C/min. and 1.3 % for the 9.9 ^{0}C/min. are observe. The highest relative density increase for reference samples was 3.3 % at 1300 ^{o}C with a heating rate of 6.6 ^{o}C/min. As can be seen from this graph, the relative density increases as the infiltration load increases. The

increase in relative density is because the nanoparticles are activated early and help to densify. Finally, the change in the relative densities of the P samples is given in Figure 4.20.

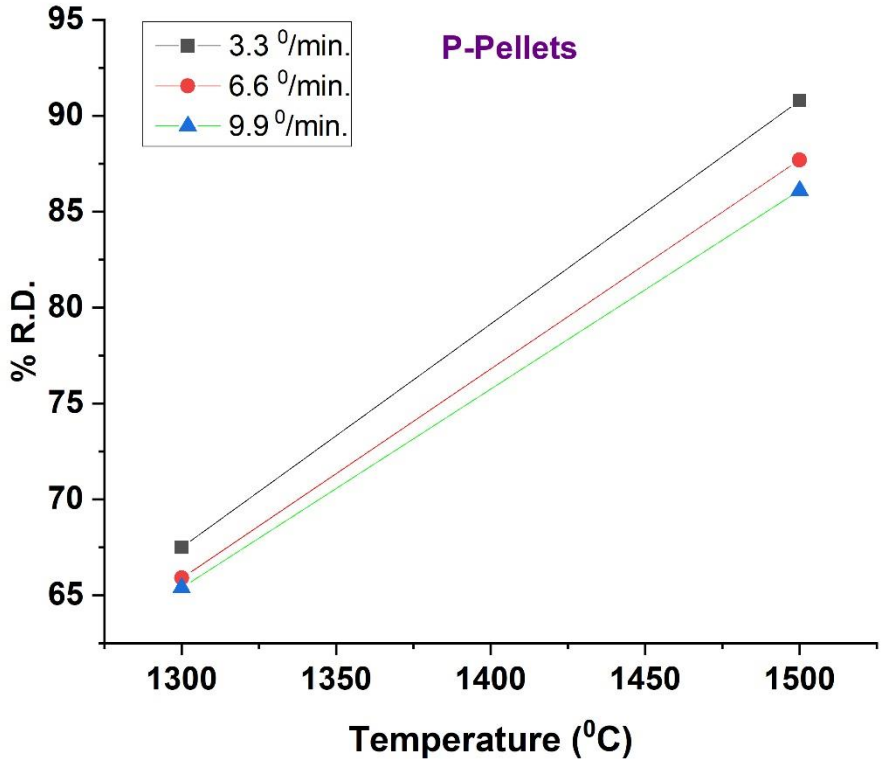

Figure 4.20. Changes in relative density values of the P pellets

Relative density trends in this graph parallel the reference and infiltrated samples. Again, as the heating rate decreases, the lines in the graph shift upwards and as the temperature increases, the densification increases. At 1300 °C, the relative density values increased from 65.4 % to 67.5 % (+3.2 %) as the heating rate decreased from 9.9 to 3.3 °C/min. . At 1500 °C, the relative density values increased from 86.1 % to 90.8 % (+5.5 %) as the heating rate fell from 9.9 to 3.3 °C/min. . At 1300 °C, relative density decreased with respect to reference samples of -1.0 % for the 3.3 °C/min., -0.3 % for the 6.6 °C/min. and +0.2 % for the 9.9 °C/min. are observed. At 1500 °C, relative density decreases or stays constant with reference samples of -3.4 % for the 3.3 °C/min., 0.0 % for the 6.6 °C/min. and -0.7 % for the 9.9 °C/min. are observed. These results showed that the sintering of the pellets obtained by pressing the powder obtained by drying the CT3000

LS SG Alumina loose powder washed with polymeric precursor solution with a uniaxial press with 200 Mpa pressure did not increase relative density. This may be because the compaction behavior of the obtained powder changes and has a lower green density due to pressing. The pellet with a lower green density will have a lower relative density when sintered at a specific temperature. Therefore, the nanoparticles may not have shown any effect.

4.5. Thermal Dilatometry Results

As will be recalled from Chapter 2, the selected infiltrated, reference, and P pellets were sintered in the horizontal dilatometer (Linseis L76150B-1600) up to 1300 and 1500 ^{0}C under static air with different constant heating rates of 3.3,5.0 and 6.6 ^{o}C/min. In this dilatometer, the load applied to the specimen was constant(0.1N).

Cylindrical pellets of approximately 8 mm in diameter and 6 mm in length were used in dilatometer experiments. Since 9.9 ^{0}C/min. heating rate in dilatometer experiments was thought to damage the silicon carbide resistors used in heating, a slower heating rate(5 ^{o}C/min.) between 3.3 ^{0}C/min. and 6.6 ^{0}C/min. was chosen for dilatometer experiments instead of a 9.9 ^{o}C/min. heating rate. In light of this information, the samples were selected according to the data obtained in the furnace experiments, and the selected samples were analyzed dilatometrically. As sample conditions, AD-13 code has been added for the pellet with a heating rate of 5 ^{o}C/min., a sintering temperature of 1300 ^{o}C, and an infiltration number of 15x. The investigated samples and their relative densities are given in Table-4.5.

Table 4.5. Archimedes' Density Results of the samples that were analyzed in a dilatometer

Code of Sample	Sintering Temperature(^{o}C)	Heating Rate(^{0}/min.)	%Relative Density
R2(D)	1300	6.6	66.7
P2(D)	1300	6.6	65.2
AD-4	1300(15x)	3.3	69.0
AD-5	1300(15x)	6.6	67.1
AD-13	1300(15x)	5.0	68.7

Considering the relative density values in the table, it was observed that the infiltrated samples successfully increased the density compared to the reference sample, but the densities of the P pellets remained below the reference sample. Samples with the same heating rate as these samples will be examined dilatometrically and evidence of the presence of earlier activated nanoparticles will be sought in the densification curves obtained from the dilatometer. The samples were heated to 1300 ^{o}C in stagnant air during the tests at a constant heating rate of 6.6 ^{o}C/min.

The calculated temperature-dependent relative linear change in length of the R2 sample is given in Figure 4.21.

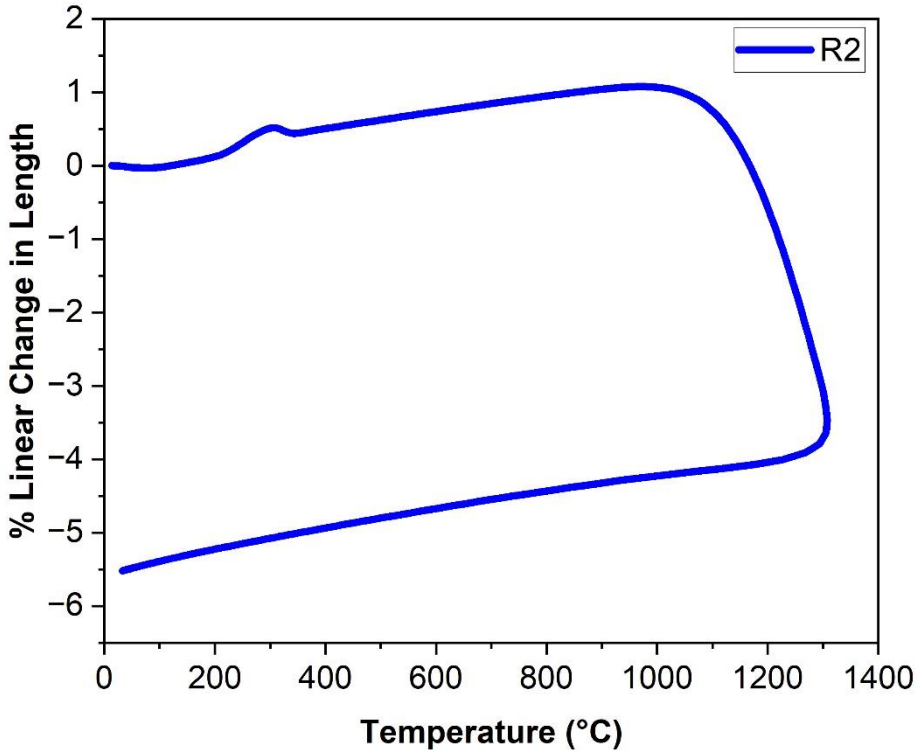

Figure 4.21. Temperature-dependent % linear change in length graph of the R2.

The green density of the pellets is usually around 55–60 vol %. This means that full densification of the ceramic will be accompanied by a large amount of shrinkage (decrease of dimensions) of approximately 35–40 vol % and 18–20 linear %. There is also a change in the shape of the powder particles with time, usually increasing in average grain size.

The shrinkage of the ceramic compact can be followed at different stages of the process using dilatometry, as shown in Figures 4.21,4.22, and 4.23. At the beginning of heating, the sample expands due to increases in the amplitude of the thermal vibration of atomic bonds.

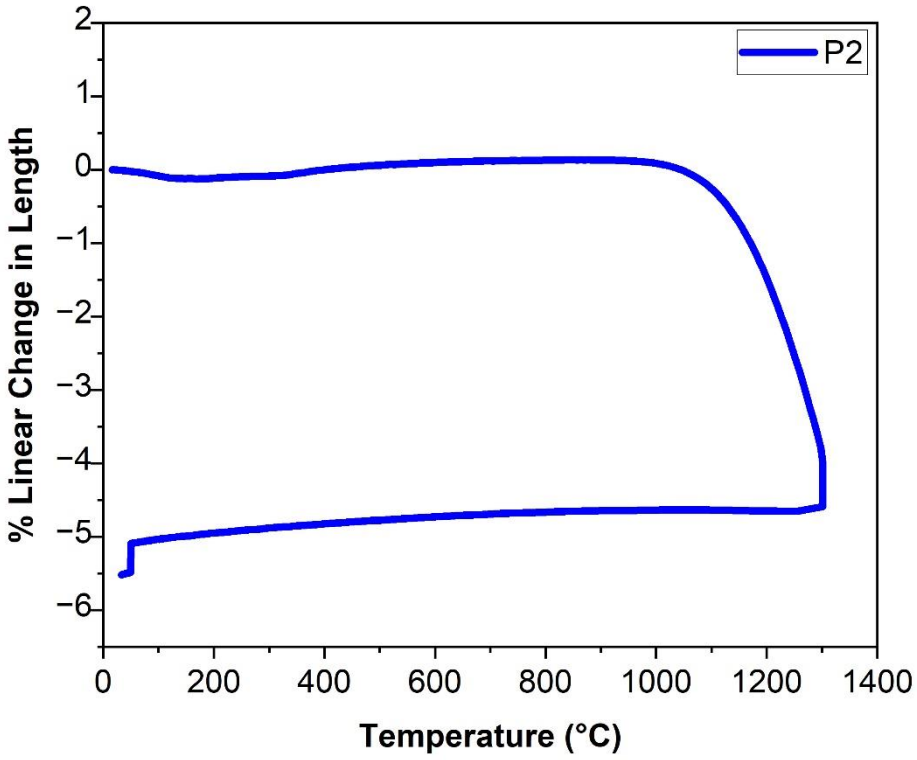

Figure 4.22. Temperature-dependent % linear change in length graph of the P2.

As can be seen from the graph, R2 expands in the temperature range of 25-1000 ^{0}C. At higher temperatures, in other words, after 1000 ^{0}C, densification commences with reduced porosity. And the R2 shrinks at these temperature ranges. As can be seen from the graph, the relative shrinkage of the pellet is approximately 5.5 %. It should be remembered that this sample is the reference sample, and it is not bisque-fired. Since the heat treatment temperature is far from the sintering temperature, this % linear shrinkage is normal. The dilatometric curve of the P2 sample is given in Figure 4.22.

As expected from a typical dilatometer curve, as seen in the first graph, the pellet similarly expands in the 25-1050 ^{o}C temperature range. It is seen that the pellet shrinks with the decrease of pores and densification. The permanent shrinkage in the pellet is 5.1%. While obtaining this sample in the first stage, the powder is obtained by mixing

CT3000 LS SG Alumina powder with a polymeric solution and keeping it in an oven at 300 ^{o}C for 3 hours. Afterward, a uniaxial press with 200 Mpa pressure brings this powder into pellet form. This sample has less permanent shrinkage compared to the reference sample because of the change in the compaction behavior of the powder. Low green density decreases the relative density value reached after densification.

The data obtained from the furnace and dilatometer experiments show that the P samples did not provide the expected relative density increase. The dilatometric curve of the AD-5 sample is given in Figure 4.23.

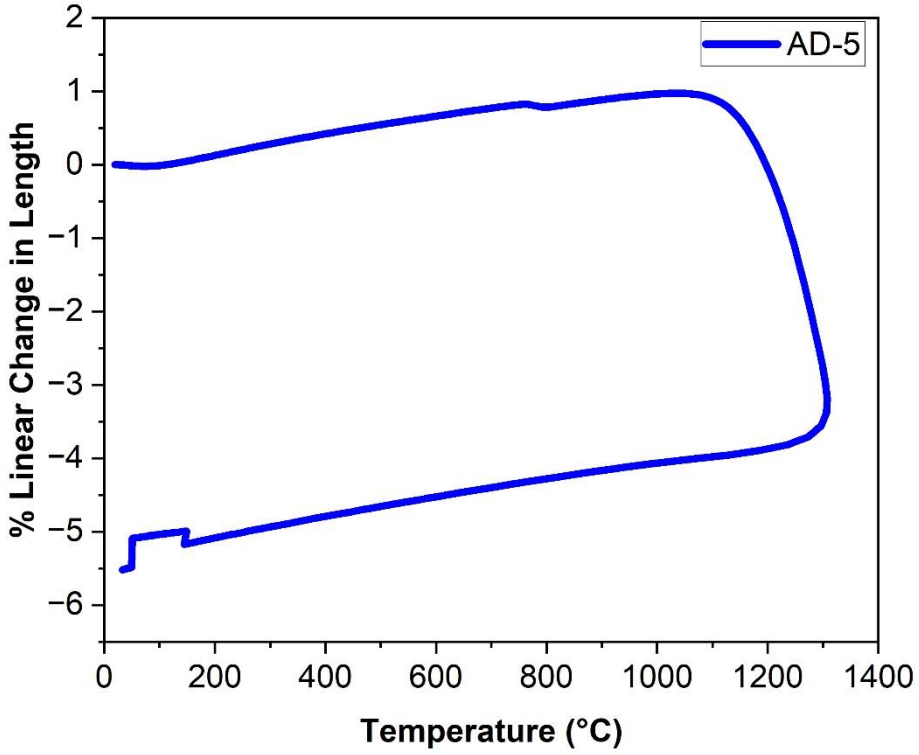

Figure 4.23. Temperature-dependent % linear change in the length graph of the AD-5.

The dilatometer graph of the AD-5 pellet is similar to the dilatometer graph of the R2 and P2 pellets. The chart shows that the pellet undergoes expansion up to approximately 1050 ^{0}C. After this temperature, the necks grow, the porosity decreases, and densification occurs. Therefore, the pellet shrinks. The amount of permanent shrinkage is approximately 5.6 %. If the preparation of the AD-5 sample is remembered, CT3000 LS SG Alumina powder was turned into pellets with a uniaxial press at 200 Mpa

pressure. Then the formed pellet was bisque fired at 1100 ºC for 1 hour. The polymeric solution prepared on the formed scaffold was infiltrated 15 times. In other words, nanoparticles are precipitated at temperatures close to sintering temperatures in the structure of the AD-5 sample, and these nanoparticles will be activated earlier due to their fineness and high surface area, enabling earlier neck formation and growth, resulting in a decrease in porosity, and sintering at lower temperatures. Accordingly, the AD-5 pellet has shrunk slightly more than the other two samples. In this section, the temperature-dependent shrinkage behavior of the pellets was investigated. The next part will analyze the shrinkage rate, densification rate and relative density change of the selected samples.

The temperature-dependent shrinkage rate graph of R2, P2, and AD-5 samples is given in Figure 4.24.

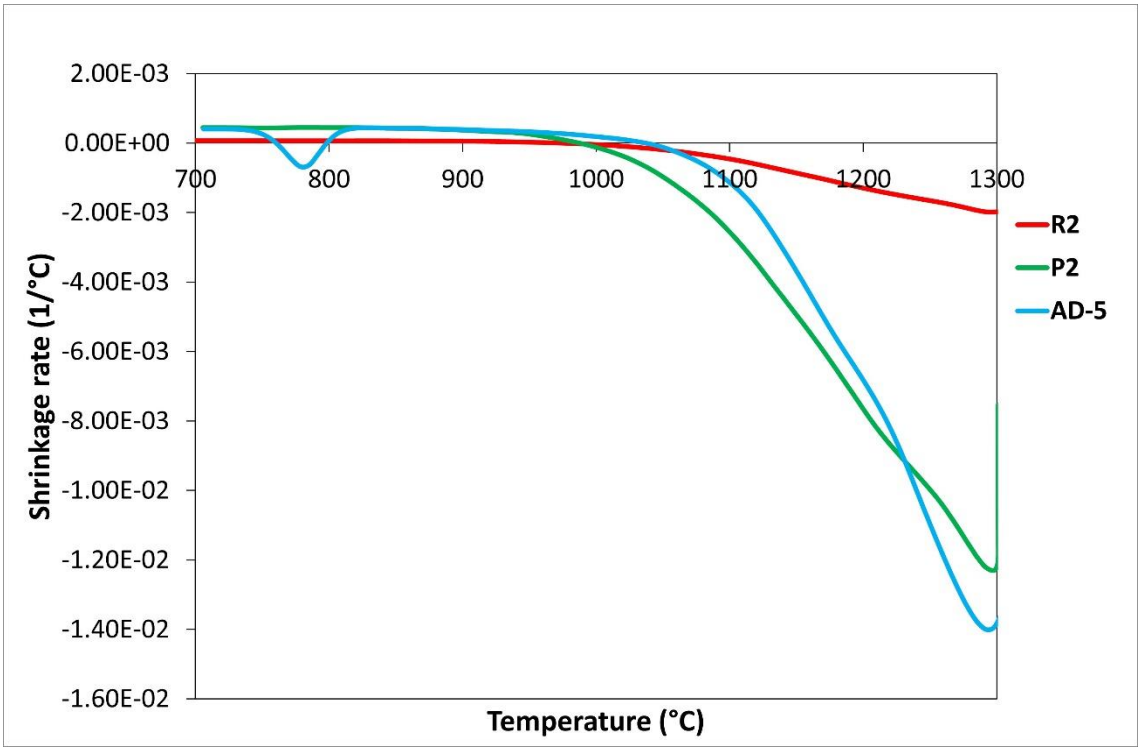

Figure 4.24. The temperature-dependent shrinkage rate graph of R2, P2, and AD-5 samples

The R2 sample begins to shrink at about 1042 ºC, and after this temperature, the rate of shrinkage increases, reaching a maximum of 1292 ºC. The P2 sample starts to shrink at about 1000 ºC, and the shrinkage rate reaches its maximum at 1298 ºC. A different behavior is observed in the AD-5 sample. The graph shows two peaks, the first

at 778 ºC, indicating that the nanoparticles have become active, as expected. Then, the shrinkage begins at 996 ºC for the second peak, and the shrinkage rate reaches a maximum of 1292 ºC. The AD-5 reference sample started to shrink earlier than R2, and the shrinkage rate's maximum value was greater than that of the R2 and P2 samples. As stated before, it can be seen from the graph that the P2 sample starts to shrink at 1000 ºC, but the point where the shrinkage rate reaches its maximum is lower than that of AD-5. The shrinkage rate data shows that the AD-5 sample started to shrink early, and the maximum shrinkage rate was higher than the other two samples. In this case, it is thought that nanoparticles play a role. But for more detailed information, temperature-dependent relative density change and densification rate of samples are shown in Figure 4.25.

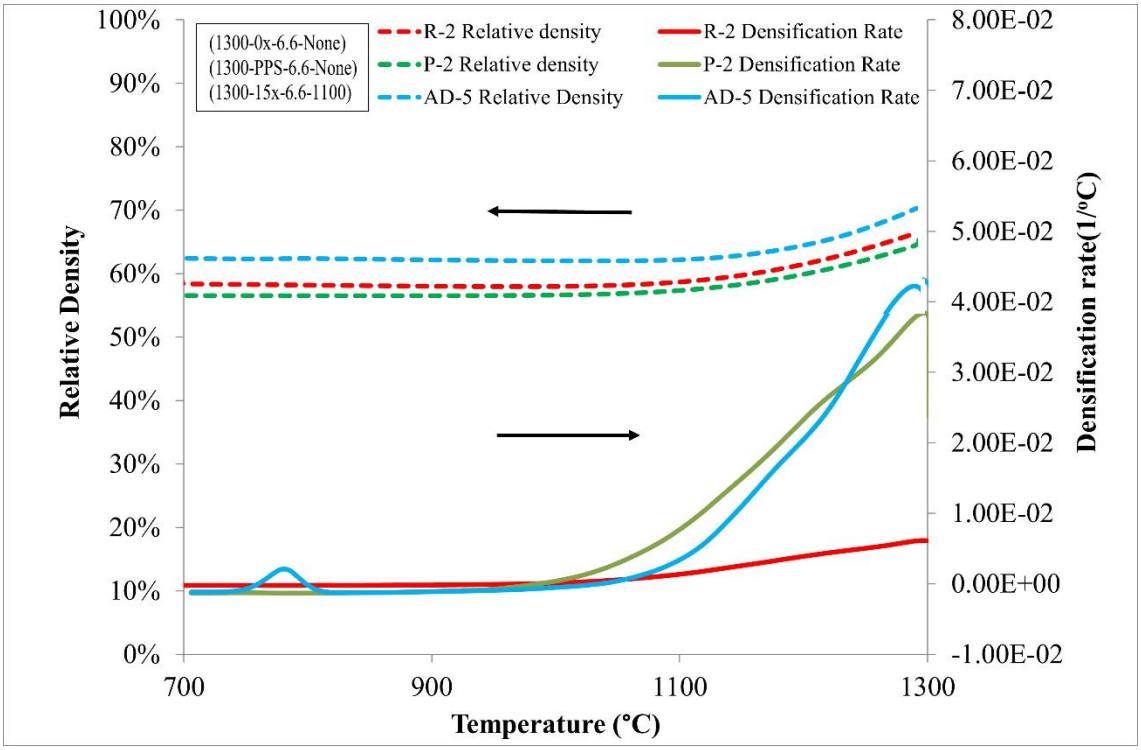

Figure 4.25. Relative density and densification rate curve of R1, P2, and AD-5

According to the published data from the manufacturer, the sintering temperature of CT3000 LS SG Alumina powder is about 1600 ºC. Since 1300 ºC is selected as the heat treatment temperature in the graph, no sample has reached total density, and all values are below 70%. At 1300 ^{0}C, The sample with the highest relative density value of 70% was AD-5. On the other hand, at 1300 ^{0}C, P2 reached the lowest relative density value of 64 %. The shrinkage rate curves mention that α-alumina nanoparticles are loaded

in the AD-5 sample. These nanoparticles become active earlier than the other particles because of their higher surface area and higher reactivity at these heat treatment temperatures. Functional nanoparticles provide earlier neck formation and growth. Therefore, at lower temperatures, it is seen that the porosity is reduced, and a higher relative density value is obtained. In the P2 sample, it is seen that mixing the nanoparticles with the CT3000 LS SG powder at the beginning of the process reaches dedensification rather than densification. This is thought to be due to the change in the compaction behavior of the powder.

When the graphs are examined, it is seen that the R2, P2, and AD-5 samples show similar trends during the heat treatment at 1300 ^{o}C in terms of relative density. Within the three samples, the trend is so identical that there is almost parallelism.

On the other hand, if the densification curves are examined in the R2 sample, there is an increase in the densification rate at 1042 ^{0}C, and the densification rate reaches its maximum value at 1300 ^{o}C. The increase in the densification rate of the P2 sample started earlier than the reference sample, as expected, at about 996 ^{o}C, but the relative density increase was not as expected. The maximum densification rate for P2 was about 1298 ^{o}C. Finally, there is a small bump on the densification rate curve at around 778 ^{o}C in the curve for the AD-5 sample. The reason for the formation of this bump in the densification rate curve is seen as the activeness of the α-alumina nanoparticles in the AD-5. Other particles in AD-5 were active at about 1000 ^{o}C, and the densification rate increased after this temperature and reached its maximum speed at 1292 ^{o}C.

In line with this information, following the purpose of the study, the presence of nanoparticles loaded on the AD-5 sample was proven by the heat treatments applied to the powders and XRD measurements in the 3.1 Powder characterization heading. Then, since the sintering behavior of the ceramic compacts is continuously monitored with a dilatometer, the temperature-dependent % linear length change, shrinkage rate,% relative density, and densification rate curves obtained from the dilatometer measurements are analyzed. As a result, the shrinkage rate and densification rate curves of the AD-5 sample show that the AD-5 sample is active at 780 ^{0}C. And it has reached the maximum relative density value of 70 %.

At the same time, the ultimate shrinkage rate and maximum densification rate are seen in the AD-5 sample. As a result, all this information shows that the nanoparticles are effective in the densification process in the α-alumina nanoparticles infiltrated sample. SEM secondary electron images of R2 are given in Figure 4.26.

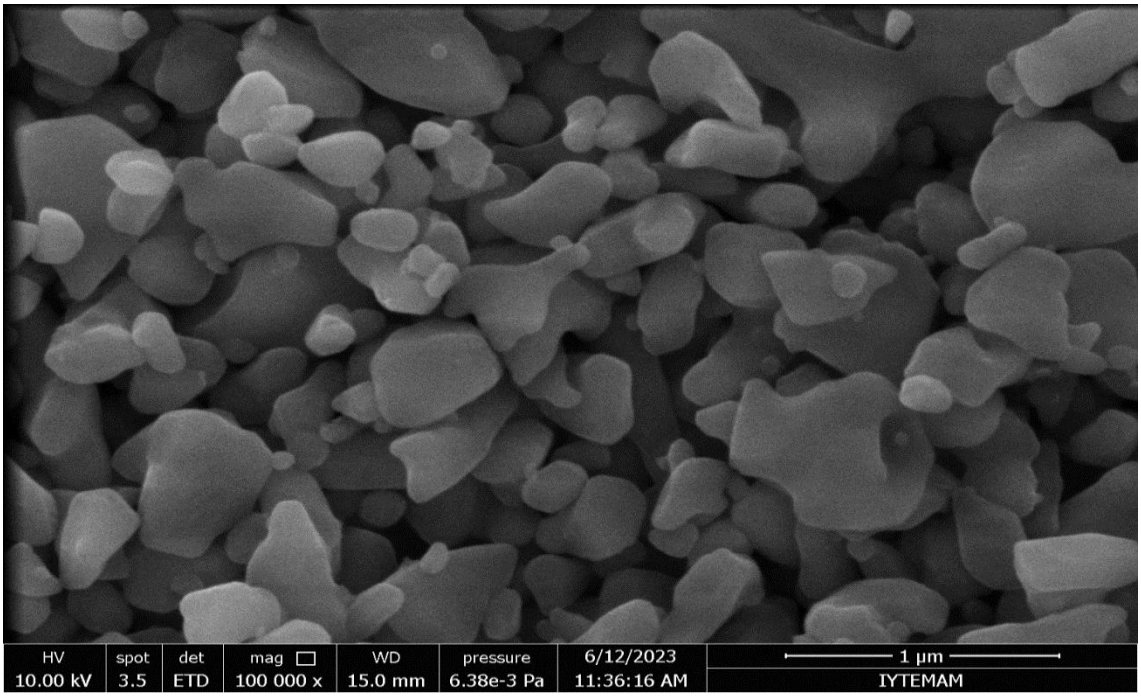

Figure 4.26. SEM secondary electron images of the fracture surface of the R2

Upon examination of the SEM secondary electron image in the R2 sample, a notable observation is the absence of neck formation. It becomes apparent that the particles within the sample have not yet established contact with each other. This lack of particle bonding is particularly evident as pores are still discernible within the microstructure. Regrettably, it is evident that the R2 sample did not achieve the anticipated level of densification. The absence of neck formation and the persistence of pores suggest that the sintering process in the R2 sample fell short of reaching the desired level of consolidation. Sintering is a critical stage in ceramics processing where particles are expected to fuse and form cohesive bonds, resulting in a reduction in porosity and an increase in density. The incomplete densification observed here could be attributed to various factors, such as suboptimal sintering temperature, inadequate sintering time, or a particle size distribution that hinders effective particle-to-particle contact. Addressing the densification issue in the R2 sample may necessitate adjustments in the sintering parameters or a reevaluation of the powder characteristics and processing conditions to achieve the desired microstructure and material properties. This careful analysis and diagnosis of the sintering process are essential steps in optimizing ceramic materials for their intended applications.

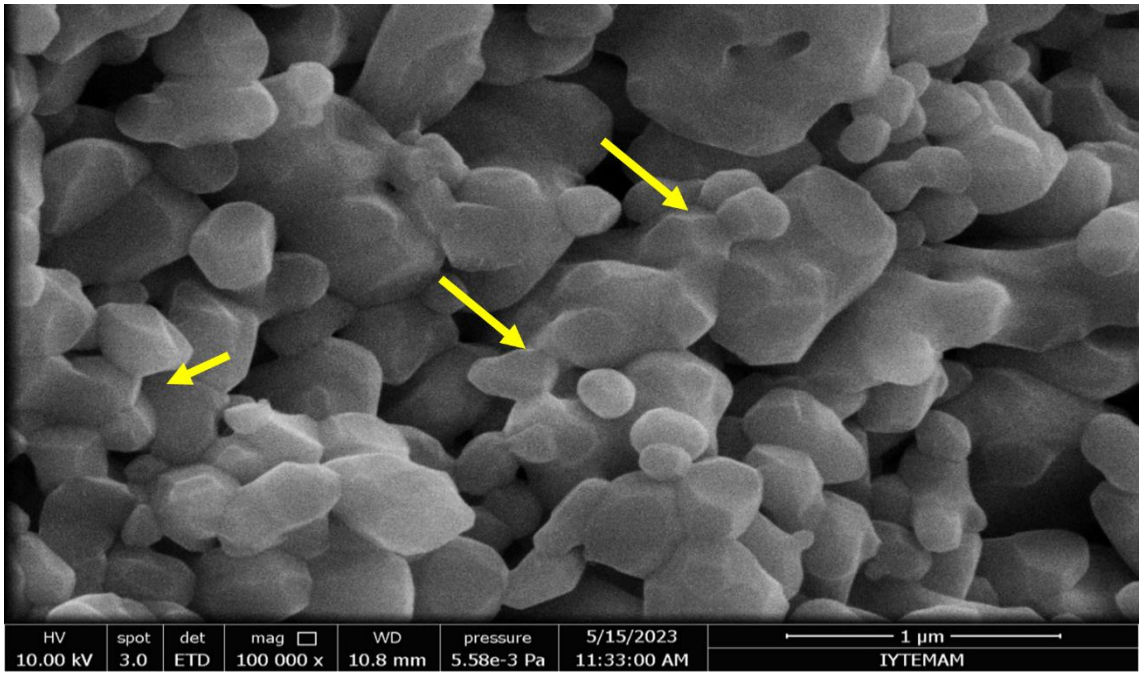

Figure 4.27. SEM secondary electron images of the fracture surface of the AD-5

In the examination of the AD-5 sample through SEM secondary electron imaging, a noteworthy phenomenon comes to light: neck formation and neck growth. The formed necks are indicated by yellow arrows. This process signifies the successful bonding and consolidation of individual particles within the sample. Consequently, there is a noticeable reduction in the presence of pores within the material's structure. This observation reflects a critical advancement in the densification of the AD-5 sample. As the sintering process progresses in the AD-5 sample, it becomes evident that the particles are not only forming necks but also undergoing a transformation in their shape. This shape change is a remarkable indication of the dynamic changes occurring within the material during sintering. These alterations in particle morphology can be attributed to the localized melting and subsequent recrystallization that takes place during sintering, ultimately leading to the formation of necks and alterations in particle geometry.

Comparatively, it is evident that the AD-5 sample has achieved a higher level of densification when contrasted with the R2 sample. This enhanced densification is a testament to the efficiency of the sintering process employed in the AD-5 sample, where effective particle bonding and reduced porosity have been achieved. The success of the AD-5 sample in achieving a superior level of densification underscores the importance of optimized sintering conditions, including temperature, time, and particle characteristics,

in ceramics processing. The contrasting outcomes between the R2 and AD-5 samples highlight the critical role of process control and material selection in ceramics manufacturing. The systematic examination of microstructural changes through SEM imaging provides valuable insights into the sintering process, allowing for refinements in processing parameters and the attainment of desired material properties. These findings not only contribute to our understanding of ceramics processing but also open avenues for the tailored design of ceramics to meet specific performance requirements in various applications.

CHAPTER 5

CONCLUSION

The sintering process of advanced ceramic powders, specifically alumina, is influenced by various factors such as grain size and surface area, resulting in a temperature range of 1000-1600 °C. CT3000 LS SG alumina stands out among these powders due to its fine grain size and high surface area. When sintered at 1500 °C, CT3000 LS SG alumina powder achieved a theoretical density of 98%. This study aims to lower the densification temperature of CT3000 LS SG alumina powder to reduce processing costs while examining the densification and sintering behavior of alumina scaffolds infiltrated with nanoparticles. A two-step heat treatment and infiltration technique has reached the required density at lower temperatures. The infiltrated polymer precursor solution includes Al^{+3} ions, and alumina nanoparticle precipitation is expected after decomposition. Alumina scaffolds were infiltrated using a series of cycles (5 or 15 times) to increase density. Three distinct groups were established for this purpose: infiltrated scaffolds, reference pellets, and pellets formed via E-powder. All samples were compressed under 200 MPa pressure. Infiltrated scaffolds were initially bisque-fired at 1100 ^{o}C to create Alumina scaffolds, which were then subjected to infiltration with varying cycles. The numerous infiltration and drying cycles aimed to precipitate alumina nanoparticles to the pores, facilitating densification at lower temperatures. The samples were then sintered in a horizontal dilatometer and box kiln at different temperatures and heating rates.

In contrast, reference pellets and pellets formed via E-powder were not bisque-fired. They were only sintered under the same conditions as the corresponding samples using the horizontal dilatometer and box kiln. The experiments conducted in the furnace resulted in the selection of samples exhibiting relative density increase based on the infiltration cycle, heating rate, and temperature.

When the temperature-dependent relative density graphs of furnace-sintered pellets are examined, the relative density increases with decreasing heating rate and increasing sintering temperature in the reference samples. The infiltrated and "P" samples also show a similar trend. Also, when the same graphs are examined, it is seen that the relative density values increase as the infiltration number increases in the infiltrated

samples. It is seen that the relative density values of the "P" samples are lower than the reference samples. In light of this information, the 15 times infiltrated AD-5 sample, where the highest density was observed, the corresponding reference sample R2 and finally, the P2 sample was analyzed in a horizontal dilatometer.

Temperature-dependent densification rate curves and relative density change curves were obtained using a horizontal dilatometer. These curves revealed a bump in the densification rate curve of the 15x infiltrated AD-5 sample, indicating early activation of the nanoparticles. In SEM secondary electron images, neck formation and growth were observed in the AD-5 sample, leading to decreased pores.

Additionally, changes in particle shape were noted. The AD-5 sample exhibited better densification compared to the R2 sample. These findings suggest that the density of the AD-5 sample increased compared to the R2 sample, although further density improvement requires enhanced infiltration cycles. The relative density values of the P2 sample were observed to be lower than those of the reference samples. These results demonstrate that loading the nanoparticles through infiltration and bisque firing processes is more advantageous than using pellets obtained with E-powder.

For future work, the number of infiltrations can be increased to increase the relative density further, and the pore size of alumina scaffolds can be examined by mercury porosimetry to investigate how capillary forces affect the infiltration process. The activation energies of infiltrated alumina scaffolds can be calculated. And finally, the information learned here is used in solid oxide fuel cells. It can be used to study the densification and sintering behavior of Gadolinia doped ceria (GDC) powder.

REFERENCES

1. Barsoum, M. W. *Fundamentals of Ceramics*. CRC Press, Taylor &; Francis Group, 2020.

2. Rahaman, M. N. *Ceramic Processing and Sintering*. CRC Press, 2017

3. Richerson, D. W. *Modern Ceramic Engineering*. CRC Press, 2015.

4. Advanced ceramics market, Regional Outlook 2023 - 2032. Retrieved from https://www.precedenceresearch.com/advanced-ceramics-market.(05.07.2023 14.38).

5. Yalamac, E. Sintering, co-sintering, and microstructure control of oxide-based materials: Zirconia, alumina, spinel, alumina-zirconia, and spinel-alumina, *İzmir Institute of Technology*, 2010, İzmir-Turkey.

6. Li, J., &; Ye, Y. Densification and grain growth of Al_2O_3 nanoceramics during Pressureless Sintering. *Journal of the American Ceramic Society*, 2006, 89(1), 139–143. doi:10.1111/j.1551-2916.2005.00654.x

7. Echeberria, J., Tarazona, J., He, J. Y., Butler, T., & Castro, F. Sinter-hip of α-alumina powders with sub-micron grain sizes. *Journal of the European Ceramic Society*, 2002, 22(11), 1801–1809. doi:10.1016/s0955-2219(01)00510-6

8. Yu, H., Xu, Z., Wei, Z., Chen, Y., Li, J.; Luo, L. Effect of talc and Titania on alumina ceramics' microstructure and mechanical properties. *International Journal of Applied Ceramic Technology, 2017, 15*(3), 633–642. doi:10.1111/ijac.12827

9. He, W., Ai, Y., Liang, B., Chen, W., Liu, C. Effects of La_2O_3 and Nb_2O_5 Dopants on the microstructural development and fracture toughness of Al_2O_3 ceramic. *Materials Science and Engineering: A*, 2018, 723, 134–140. doi:10.1016/j.msea.2018.03.057

10. Liu, J., &; Wu, B. Effects of Eu_2O_3 addition on microstructure, grain-boundary cohesion and wear resistance of high-alumina ceramics. *Journal of Alloys and Compounds*, 2017, 695, 2324–2329. doi:10.1016/j.jallcom.2016.11.099

11. Odaka, A., Yamaguchi, T., Hida, M., Taruta, S., Kitajima, K. Fabrication of submicron alumina ceramics by Pulse Electric Current Sintering using M^{2+} (M=Mg, Ca, Ni)-doped alumina nanopowders. *Ceramics International, 2009, 35*(5), 1845–1850. doi:10.1016/j.ceramint.2008.10.007

12. Wu, T., Zhou, J., &; Wu, B. Effect of Y_2O_3 on acid resistance of alumina ceramic. *Ceramics International*, 2017, 43(6), 5102–5107. doi:10.1016/j.ceramint.2017.01.023

13. Yang, R., Qi, Z., Gao, Y., Yang, J., Zhou, Y., Liu, H., Jiao, J. Effects of alumina sols on the sintering of α-alumina ceramics. *Ceramics International*, 2020, 46(13), 20865–20870. doi:10.1016/j.ceramint.2020.05.125

14. Wang, Y., Liu, H., Cheng, H.,; Wang, J. Densification behavior and microstructure of mullite obtained from diphasic Al_2O_3–SiO_2 gels. *Ceramics International*, *2014*, *40*(8), 12789–12796. doi:10.1016/j.ceramint.2014.04.133

15. Ananthakumar, S., Menon, A. R. R., Prabhakaran, K., Warrier, K. G. K. Rheology and packing characteristics of alumina extrusion using boehmite gel as a binder. *Ceramics International*, *2001*, 27(2), 231–237. doi:10.1016/s0272-8842(00)00070-5

16. Ananthakumar, S., Raja, V., Warrier, K. G. K. Effect of nanoparticulate Boehmite Sol as a dispersant for slurry compaction of alumina ceramics. *Materials Letters*, *2000*, *43*(4), 174–179. doi:10.1016/s0167-577x(99)00255-4

17. Herring, C. Effect of change of scale on sintering phenomena. *Journal of Applied Physics*, *1950*, *21*(4), 301–303. doi:10.1063/1.1699658

18. Rhodes, W. H. Agglomerate and particle size effects on sintering yttria-stabilized zirconia. *Journal of the American Ceramic Society*, *1981*, *64*(1), 19–22. doi:10.1111/j.1151-2916.1981.tb09552.x

19. Lange, F. F. Sinterability of agglomerated powders. *Journal of the American Ceramic Society*, *1984*, *67*(2), 83–89. doi:10.1111/j.1151-2916.1984.tb09620.x

20. R.T. Tremper and R. S. Gordon, '*Agglomeration Effects on the Sintering of Alumina Powders Prepared by Autoclaving Aluminum Metal*", pp. 153-76 in Ceramic Processing Before Firing. Edited by G. Onoda and L. L. Hench. Wiley, New York, 1978

21. Lange, F. F. Cheminform abstract: Powder Processing Science and technology for increased reliability. *ChemInform*, *1989*, *20*(15). doi:10.1002/chin.198915379

22. Readey, D. W. Mass transport and sintering in impure Ionic solids. *Journal of the American Ceramic Society*, *1966*, *49*(7), 366–369. doi:10.1111/j.1151-2916.1966.tb13286.x

23. Bagley, R. D., Cutler, I. B., Johnson, D. L. Effect of TiO_2 on initial sintering of Al_2O_3. *Journal of the American Ceramic Society*, *1970*, *53*(3), 136–141. doi:10.1111/j.1151-2916.1970.tb12055.x

24. Kingery, W. D. Densification during sintering in the presence of a liquid phase. I. *Theory. Journal of Applied Physics, 1959, 30*(3), 301–306. doi:10.1063/1.1735155

25. Chen, C., Nasrallah, M., Anderson, H. *Synthesis and characterization of YSZ thin film electrolytes.* Solid State Ionics, 1994, 70–71, 101–108. doi:10.1016/0167-2738(94)90293-3

26. C. Durucan, A. Öztürk, M. Timuçin," Ceramic Materials METE451", Ankara, Turkey: METU, *Metallurgical and Materials Engineering Department*," 2009.

27. Retrieved from https://ceramics.org/about/what-are-engineered-ceramics-and-glass/structure-and-properties-of-ceramics/ (05.07.2022 21.37)

28. Cho, S.-J., Hockey, B. J., Lawn, B. R., & Bennison, S. J. Grain-size and R-curve effects in the abrasive wear of alumina. *Journal of the American Ceramic Society, 1989, 72*(7), 1249–1252. doi:10.1111/j.1151-2916.1989.tb09718.x

29. Saud, A. N., Majdi, H. Sh., Saud, S. N. Synthesis of nano-alumina powder via recrystallization of ammonium alum. *Cerâmica*, 2019, 65(374), 236–239. doi:10.1590/0366-69132019653742636

30. Inventions new and interesting. *Scientific American*, 1919, 120(4), 80–80. doi:10.1038/scientificamerican01251919-80

31. Kühn, G. *Crystals (growth, properties, and applications),* vol. 9 Modern Theory of Crystal Growth I: Springer-Verlag Berlin, Heidelberg, New York 1983, 148 Seiten, Preis: DM 88,—. Crystal Research and Technology, 1984, 19(1), 26–26. doi:10.1002/crat.2170190106

32. Carlos de Souza Santos, J., de Souza Rangel, A. Introdução à Análise de Investimento, 2018, doi:10.24824/978854441327.2

33. Cava, S., Tebcherani, S. M., Souza, I. A., Pianaro, S. A., Paskocimas, C. A., Longo, E., Varela, J. A. Structural characterization of phase transition of Al_2O_3 nanopowders obtained by polymeric precursor method. *Materials Chemistry and Physics,2007, 103*(2–3), 394–399. doi:10.1016/j.matchemphys.2007.02.046

34. Truex, T. J., Hammerle, R. H., & Armstrong, R. A. The thermal decomposition of aluminum sulfate. *Thermochimica Acta*, 1977, 19(3), 301–304. doi:10.1016/0040-6031(77)80005-1

35. Tabesh, S., Davar, F., Loghman-Estarki, M. R.. Preparation of γ-Al_2O_3 nanoparticles using the modified sol-gel method and its use for the adsorption of lead and cadmium ions. *Journal of Alloys and Compounds, 2018,* 730, 441–449. doi:10.1016/j.jallcom.2017.09.246

36. Hosseini, S. A., Niaei, A., & Salari, D. Production of γ-Alumina from Kaolin. *Open Journal of Physical Chemistry*, 2011, 01(02), 23–27. doi:10.4236/ojpc.2011.12004

37. Edomwonyi-Otu, L. C., Aderemi, B. O., Edomwonyi-Otu, O., Simo, A., Maaza, M. Alum production from some Nigerian kaolinite deposits. *International Journal of Engineering Research in Africa, 2012,* 7, 13–19. doi:10.4028/www.scientific.net/jera.7.13

38. Dodoo-Arhin, D., Nuamah, R. A., Agyei-Tuffour, B., Obada, D. O., Yaya, A. AWASO bauxite red mud-cement based composites: Characterization for pavement applications. *Case Studies in Construction Materials, 2017,* 7, 45–55. doi:10.1016/j.cscm.2017.05.003

39. Grant., C., C. Barry. Norton, M. *Ceramic materials: Science and engineering, 2016,* Springer-Verlag New York.

40. Ramogayana, B., Santos-Carballal, D., Maenetja, K. P., de Leeuw, N. H., Ngoepe, P. E.. Density functional theory study of ethylene carbonate adsorption on the (0001) surface of aluminum oxide α-Al_2O_3. *ACS Omega*, 2021, 6(44), 29577–29587. doi:10.1021/acsomega.1c03771

41. Retrieved from https://www.sciencedirect.com/topics/chemistry/alpha-aluminium-oxide(01.07.2023,13.58)

42. Ishak, N. F., Hashim, N. A., Othman, Mohd. H., Monash, P., Zuki, F. M. Recent progress in the hydrophilic modification of alumina membranes for protein separation and purification. *Ceramics International*, 2017, 43(1), 915–925. doi:10.1016/j.ceramint.2016.10.044

43. Coble, R. L. Sintering alumina: Effect of atmospheres. *Journal of the American Ceramic Society, 1962, 45*(3), 123–127. doi:10.1111/j.1151-2916.1962.tb11099.x

44. Rahaman, M. N. Sintering of ceramics, 2018, Boca Raton, FL: CRC Press.

45. Srolovitz, D. J., Anderson, M. P., Sahni, P. S., & Grest, G. S. Computer simulation of grain growth—II. grain size distribution, topology, and local dynamics. *Acta Metallurgica*, 1984, 32(5), 793–802. doi:10.1016/0001-6160(84)90152-4

46. Anderson, M. P., Srolovitz, D. J., Grest, G. S., & Sahni, P. S. Computer simulation of grain growth—I. Kinetics. *Acta Metallurgica*, 1984, 32(5), 783–791. doi:10.1016/0001-6160(84)90151-2

47. Tekin, S. Sintering and densification behavior of GDC infiltrated porous GDC scaffolds, *İzmir Institute of Technology*, 2021, İzmir-Turkey.

48. Retrieved from https://www.tainstruments.com/products/dilatometers/(03.07.2023).

49. Retrieved from https://analyzing-testing.netzsch.com/en/contract-testing/methods/dilatometry-dil (03.07.2023).

50. Hunkel, Martin, Holger Surm, and Matthias Steinbacher. "*Dilatometry.*" Handbook of Thermal Analysis and Calorimetry 6, 2018, 103-29.https://doi.org/10.1016/B978-0-444-64062-8.00019-X.

51. Hillman, S. H., & German, R. M. Constant heating rate analysis of simultaneous sintering mechanisms in Alumina. *Journal of Materials Science*, 1992, 27(10), 2641–2648. doi:10.1007/bf00540683

52. Legros, C., Carry, C., Bowen, P., Hofmann, H. Sintering of transition alumina: Effects of phase transformation, powder characteristics, and thermal cycle. *Journal of the European Ceramic Society*, 1999, 19(11), 1967–1978. doi:10.1016/s0955-2219(99)00016-3

53. Sındıraç, C., Çakırlar, S., Büyükaksoy, A., Akkurt, S. Lowering the sintering temperature of solid oxide fuel cell electrolytes by infiltration. *Journal of the European Ceramic Society, 2019,* 39(2–3), 409–417. doi:10.1016/j.jeurceramsoc.2018.09.029

54. Buyukaksoy, A., Birss, V. I. Highly active nanoscale Ni-yttria-stabilized zirconia anodes for micro-solid oxide fuel cell applications. *Journal of Power Sources, 2016,* 307, 449–453. doi:10.1016/j.jpowsour.2015.12.022

55. Toniolo, N., Rincón, A., Avadhut, Y. S., Hartmann, M., Bernardo, E., Boccaccini, A. R. Novel geopolymers incorporate Red Mud and waste glass cullet. *Materials Letters*, 2018, 219, 152–154. doi:10.1016/j.matlet.2018.02.061

56. Retrieved from http://science.jrank.org/pages/1182/CapillaryAction.html (05.07.2023 21.49)

57. Fang, H.-Y., Chaney, R. C. *Introduction to Environmental Geotechnology*, 2016, doi:10.1201/9781315374734

58. Cospheric. (2012). Retrieved from https://microspheres.us/porous-ceramics-polyethylene-microspheres/ (05.07.2023 21.53)